Transient force generation during impulsive rotation of wall-mounted panels

Alexis Pierides, Amir Elzawawy† and Yiannis Andreopoulos

Experimental Aerodynamics and Fluid Mechanics Laboratory, Mechanical Engineering,
The City College of the City University of New York, New York, NY 10031, USA

Square and triangular shape actuator panels mounted on the wall of a wind tunnel beneath an air flow have been impulsively rotated with an angular velocity between 3 and 26 rad s^{-1}. A custom-designed balance was used to measure the time-dependent lift and drag forces during the deployment of the actuator, the position of which was monitored by a digital encoder. The measured forces have been compensated for inertia effects which are significant. The results indicated that all lift and drag force coefficients during the transient deployment are different than the corresponding coefficients under stationary conditions at the same deployment angle. It was found that these dynamic effects are augmented with increasing velocity ratio *Str*. The square actuator was found to have better aerodynamic performance than the triangular ones. Additional experiments within different boundary layers reveal that the generated unsteady forces on the moving panels are affected by the characteristics of the incoming boundary layers. The results showed that the thinner the boundary layer is the higher the forces are. Time-resolved flow visualization studies indicated that during the deployment of the panel the upstream turbulent boundary layer structures and the free stream fluid are decelerated and squeezed in the longitudinal direction as they approach the moving plate. A very thin and highly sheared wall layer develops over the moving panel, it generates a substantial amount of vorticity and it subsequently separates from the three edges of the panel to form a large-scale ring-like vortical structure which is responsible for the transient augmentation of the aerodynamic forces. This structure consists of wrapped around separated shear layers which contain pockets of compressed eddies and free stream fluid originated in the upstream incoming boundary layer and free stream. A horseshoe vortex starts to form over the moving plate and during the final stages of deployment it has been moved upstream while the incoming boundary layer turbulent structures are pushed and diverted upwards.

Key words: aerodynamics, swimming/flying, vortex flows

1. Introduction

Most of the previous work on the flow around moving panels was focused on flow control applications (Ho & Tai 1998; Ho *et al.* 2003) through vorticity manipulation

† Email address for correspondence: amir.elzawawy@vaughn.edu

(Anderson *et al.* 1998; Triantafyllou *et al.* 2003) or thrust-generating configurations inspired by biological designs (Ellington 1984; Ellington *et al.* 1996; Birch & Dickinson 2001) and the motion of birds (Maxworthy 1981; Wang 2005) or fish and other marine mammals. Flapping of wings (Freymuth 1988), fins, tails or panels (Buckholtz & Smits 2006) is a characteristic of their motion which generates not only lift and thrust for forward movement, but also provides remarkable maneuvers with rapid accelerations and decelerations. Unsteady hydrodynamics or aerodynamics associated with these flows is normally characterized by moving large-scale vortex structures (Triantafyllou, Triantafyllou & Gopalkrishnan 1991; von Ellenrieder, Parker & Soria 2003; Green & Smits 2008) a characteristic which complicates understanding of the kinematics of flapping motion and the resulting unsteady vorticity production. In that respect, an interesting problem in uncovering the physics of force generation is the role of large-scale vortex dynamics and the corresponding flow topology. Some of the unsteady flow features including the effects of rotation on leading edge and wake vortex dynamics have been described in the aforementioned publications.

As an extension of this body of work involving oscillatory flows, focus is redirected toward transients associated with thin panels that rapidly emerge in time from a flat wall beneath a flow. In particular, a wind-tunnel experiment has been designed to establish the unsteady aerodynamic characteristics of flaps during their transient deployment as control surfaces under various flow conditions. To distinguish between the stationary and the rising panel, the latter shall be also referred to as an actuator. Two particular shapes of actuator flaps were investigated in the present work, one triangular and one square as shown in figure 1(*a*). These control surfaces/panels may produce aerodynamic forces during their unsteady motion that are different than their corresponding values during static operation. It is envisioned that these wall-mounted devices can be embedded on the surface of an aircraft wing that are deployed on demand through distributed control. At the end of their control cycle they can be retracted so that they are not contributing to the overall drag.

The present flow field involves an impulsively rotating low-aspect-ratio flat panel in the presence of a cross-flow and a solid wall. The effects of angular acceleration on the force generation of the rotating panels have been investigated as they interact with the incoming boundary layer and the free stream flow above. Although no previous work on this flow configuration has been identified, several insights on the flow structures can be obtained from observations of flapping motions induced by rotating wings undergoing oscillatory acceleration particularly under hovering conditions. Of interest are the low-Reynolds-number experiments of Suryadi, Ishil & Obl (2010) and Kim & Gharib (2010) in water which show a continuous pattern of shed vorticity in a vortex around the moving perimeter of the plate containing the leading edge vortex (LEV) and side tip vortices.

Substantially enhanced drag forces have been observed experimentally and theoretically in flat plates normal to the flow undergoing longitudinal acceleration during impulsive translational motion (Sarpkaya & Kline 1982; Koumoutsakos & Shiels 1996; Ringuette, Milano & Gharib 2007; Taira *et al.* 2007). Theoretical considerations show that the vorticity, which is related to circulation, is responsible for the generation of lift force exerted on solid bodies immersed in a fluid.

The rotating motion of the flap inside the viscous fluid will generate vorticity at its surface by the action of pressure gradients which will be subsequently shed into the flow field. The Navier–Stokes equations written in rotational form for a coordinate
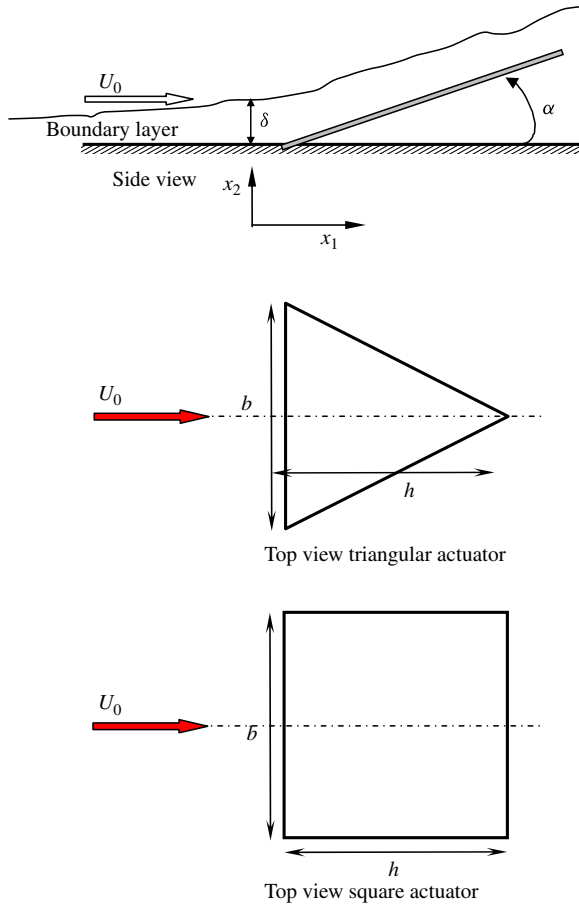
FIGURE 1. (Colour online) Flat panel actuators embedded at the wall beneath a flow.

system associated with the stationary wall in tensor notation are

$$\rho \frac{\partial U_i}{\partial t} = -\frac{\partial p}{\partial x_i} - 2\rho U_k R_{ik} + 2\mu \frac{\partial R_{ij}}{\partial x_j} \tag{1.1}$$

where R_{ij} is the rotation-rate tensor $R_{ij} = (\partial U_i/\partial x_j - \partial U_j/\partial x_i)/2 = -\varepsilon_{ijk}\Omega_k/2$, Ω_k is the vorticity and p is the total pressure. The term $2\rho U_k R_{ik}$ represents the Lamb vector. These equations when applied to the moving wall of the flap became

$$\left[\frac{\partial p}{\partial x_1}\right]_w = \left[-2\rho u_{bn2}R_{12} + 2\mu \frac{\partial R_{12}}{\partial x_2}\right]_w = [\rho u_{bn2}\Omega_3]_w - \left[\mu \frac{\partial \Omega_3}{\partial x_2}\right]_w \tag{1.2a}$$

$$\left[\frac{\partial p}{\partial x_3}\right]_w = \left[-2\rho u_{bn2}R_{32} + 2\mu \frac{\partial R_{32}}{\partial x_2}\right]_w = [\rho u_{bn2}\Omega_1]_w - \left[\mu \frac{\partial \Omega_1}{\partial x_2}\right]_w \tag{1.2b}$$

where u_{bn2} is the moving body velocity normal to its surface. The first term on the right-hand side of the above equations represents the flux of the spanwise and longitudinal vorticity which enters the flow field. It is this term which can change the moment of the vorticity field and therefore an augmented aerodynamic force can be generated.

Key flow parameters in the present flow are the Reynolds number of the flow, $Re_h = U_0 h/\nu$ and the Stokes number, $St = \omega h^2/\nu$ where ω is the frequency of deployment motion. The Stokes number expresses the square of the ratio of the size of the actuator, h, to the unsteady boundary layer thickness on the actuator, $\delta_a = (\nu/\omega)^{1/2}$. If St is large, the actuator is not strongly influenced by viscous effects, while if St is small, the flow on the actuator is strongly viscous.

The Reynolds and Stokes numbers can be combined to form a non-dimensional parameter $Str = St/Re_h = \omega h/U_0 = U_r/U_0$, where U_r is the velocity at the apex of the actuator/flap. If this parameter is considered as a ratio of two frequencies, it has significant similarities to the Strouhal number definition. The Str parameter is also related to the inverse of the Rossby number defined as $Ro = U_0/\omega h$ which is used in rotating flows. In the present context, Str has the meaning of a velocity ratio or a dimensionless angular velocity.

The present approach includes direct measurement of the time-dependent forces acting on the actuators during their transient deployment inside a boundary layer with thickness δ comparable with h. Two cases have been investigated with $h/\delta = 2$ and 0.71. Direct measurement of the forces is preferred because measuring a time-dependent three-dimensional vorticity field and integrating its moment throughout the flow appears to be a rather difficult and close to impossible task that involves tedious and possibly inaccurate operations. The effects of the deployment rate of the actuator on the force generation were also established. These measurements are accompanied by detailed flow visualization studies to understand the complex three-dimensional structure of the flow field.

2. Experimental set-up

Several new wind tunnel actuator models have been designed and fabricated for the experimental investigation. Two planform shapes were used, one triangular and one rectangular each with base $b = 10$ cm and height $h = 10$ cm and a corresponding area ratio of $1 : 2$. The motion of the actuator is provided by a servo-motor which is controlled remotely. The actuators can move at any position between 0 and 90° with the help of a digitally encoded servo-motor with 1024 positions/90°. This constituted the entire actuator system and it is built in such way so that it can accommodate actuators of various shapes, i.e. delta, square or semicircular. The base supports can also be changed to accommodate larger or smaller actuators of those shapes. In addition the actuators can be configured to deploy with their tip projecting upwind or downwind. Each of the actuators had a thickness of 1 mm and was housed in a very shallow cavity below the wind tunnel wall so that when they were not deployed their top surface was flush with the tunnel wall.

The present work requires the measurements of time-dependent aerodynamic forces. A new balance has been designed, fabricated and tested which is capable of measuring small unsteady lift and drag forces acting on the moving flaps. The major characteristics of this balance are: ability to measure lift and drag forces decoupled from each other; ability to measure lift and drag forces independent of point of application (centre of pressure); ability to measure small drag forces, a feature possible through a force multiplier arm system; ability to provide temporarily resolved measurements of forces through three small load cells of high-frequency response; and ability to provide measurements free from wind tunnel floor vibrations. The aerodynamic balance is designed to mechanically decouple the forces of drag and lift experienced by a model fastened on the square base platform and exposed to the flow
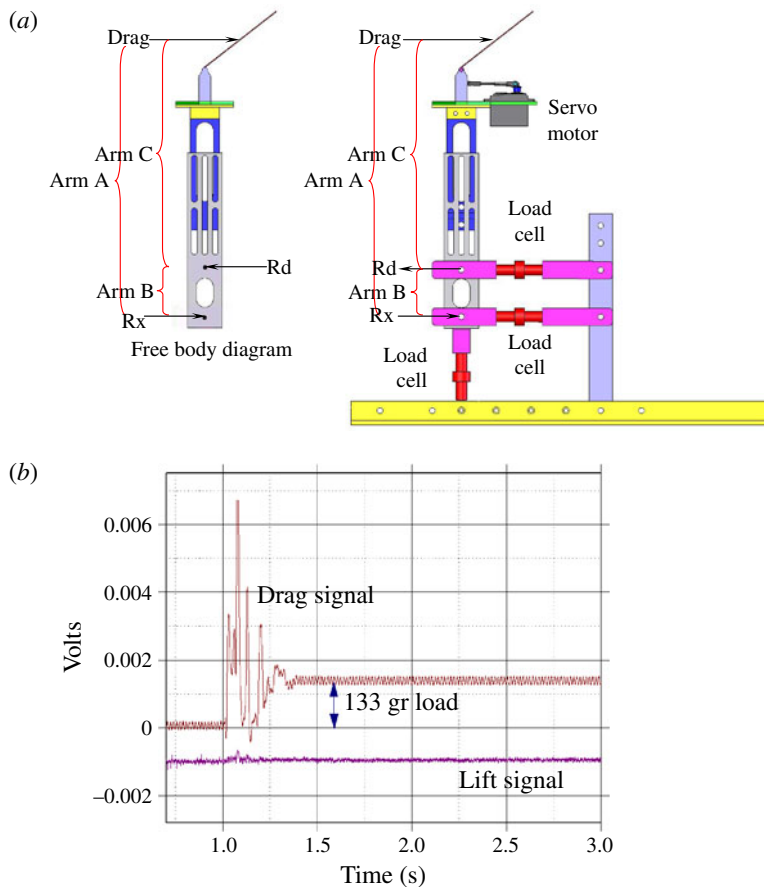
(a)

(b)

FIGURE 2. (Colour online) (*a*) Centre of pressure independent balance and free body diagram. The difference in force felt by load cells Rx and Rd is independent of arm lengths A and C. (*b*) Frequency response test of balance during sudden loading of drag force. The lift signal is shifted for clarity.

in the wind tunnel. This is achieved by first transforming the overall force (drag + lift) experienced by the model into two separate moments and then measuring the moment strength through a lever system. The advantage of this procedure is twofold. First, it decouples mechanically the two forces and therefore there is absolutely no post-testing data processing which involves calculation or data manipulation needed to separate drag and lift because each load cell only records one of the two components. Second, since there is a lever system involved in the measurement of drag, it gives us the opportunity to amplify the forces by an independent factor, giving us high signal-to-noise ratios to work with. Figure 2(*a*) shows schematics of the balance. Three Honeywell Model 34 tension and compression load cells were used to measure the local forces. Static calibrations were carried out which included the application of known forces on the actuators at known distances from the nominal centre of pressure, the recording of the corresponding voltage and eventually recovering the position of the centre of pressure.

A test to determine the frequency response of the balance system was carried out in the absence of any wind velocity. A weight of 113 g was suddenly dropped and

both signals of drag and lift were recorded. Although the magnitude of this weight represents the range of the expected aerodynamic loads acting on the panels, its actual value is immaterial for the present frequency response tests to an impulse input forcing. The applied vertical load through a pulley was acting in the direction of the drag force. The results of frequency response tests are shown in figure 2(*b*). The recorded signals clearly suggest that the two measured forces are decoupled from each other. The value of the lift signal is 1/30th of that of the drag measured during loading of the drag measuring load cell. The frequency response of the drag measuring arrangement is about 150 Hz, which is adequate to capture the time-dependent force in the present experiments during the deployment of the flap. This value has been determined by estimating the rising time of the signal to the level of 0.63 of its maximum value.

While the entire assembly, housing the actuator, its motor and the balance, must be completely detached from the wind tunnel base so that the aerodynamic forces could be transferred to the balance uncontaminated by forces from contact points with the wind tunnel wall, the tolerances between the actuator and the base have to be as small as practicable in order to allow minor movement for unobstructed measurements while avoiding excessive leakage. In order to further minimize any leakage into the wind tunnel, a thin flexible latex sheet was incorporated to seal the base while allowing for the same free movement as before.

This assembly has been placed in the wind tunnel for testing. In order to provide vibrations isolation, it rests on the laboratory floor and not on the wind tunnel floor. Details of the wind tunnel flow and the boundary layer characteristics can be found in the work by Andreopoulos & Agui (1996). Two accelerometers (DC type EGAX-25-C200001 fabricated by Entran, measurement specialties) were placed on the centre of mass of the model to assess the inertia effects on the measurements of the aerodynamic forces. One was monitoring the radial acceleration of the rotating flap, along with the projection of gravity into the radial direction, and the second was monitoring the tangential acceleration along with the projection of gravity into the tangential/azimuthal direction. The components of gravity were subtracted from the measured values in order to obtain pure aerodynamic effects. The angular location of the flap was also monitored by the feedback voltage of a potentiometer of an encoder inside the servomotor which was driving the actuator through a remote control. The first time derivative of this signal is proportional to the angular velocity and its second derivative is proportional to the angular acceleration. This information together with the acceleration signals indicated that the angular velocity of the actuator during its rotation was constant, except in the beginning and the end of the deployment for low-velocity ratio. The reader can find details of the experimental set-up in (Pierides 2011).

Several experiments were carried out with these two actuators embedded in the wind tunnel wall at different downstream locations where the boundary layers of thicknesses were $\delta = 5$ and 14 cm. The effect of deployment rate of the actuator in each of these sets of experiments was also investigated by changing the angular velocity. Their bulk flow parameters are listed in table 1.

Flow visualization experiments were also conducted with the aim of providing qualitative information on the structure of the flow field. A CW laser sheet was used to visualize the flow and a high-frame-rate CMOS camera model Phantom 710 was used to record the images with 1280×800 pixel resolution. Olive oil droplets generated through an atomizer and water vapour were introduced into the boundary

Run	$\delta = 5$ cm; $h/\delta = 2$ $Re_h = hU_0/\nu = 68\,200$; $Re_\theta = 3400$				$\delta = 14$ cm; $h/\delta = 0.71$ $Re_h = 70\,300$; $Re_\theta = 9900$	
	$h \times B$ m × m	ω rad s^{-1}	$St = \omega h^2/\nu$	$Str = \omega h/U_0$	$St = \omega h^2/\nu$	$Str = \omega h/U_0$
Square #1	0.1 × 0.1	3	2044	0.03	2109	0.03
Square #2	0.1 × 0.1	7	4769	0.07	4921	0.07
Square #3	0.1 × 0.1	15	9539	0.14	9842	0.14
Square #4	0.1 × 0.1	22	14\,308	0.21	14\,763	0.21
Square #5	0.1 × 0.1	26	16\,352	0.24	16\,872	0.24
Triangular #1	0.1 × 0.1	3	2044	0.03	2109	0.03
Triangular #2	0.1 × 0.1	7	4769	0.07	4921	0.07
Triangular #3	0.1 × 0.1	15	9539	0.14	9842	0.14
Triangular #4	0.1 × 0.1	22	14\,308	0.21	14\,763	0.21
Triangular #5	0.1 × 0.1	26	16\,352	0.24	16\,872	0.24

TABLE 1. Bulk parameters in experiments of transient deployment of actuators within a boundary layer for two different thicknesses $\delta = 5$ and 14 cm.

layer through a hole in the wall located 100 cm upstream of the rotating panel to scatter the laser light.

3. Data processing

The output signals of the three load cells, the two accelerometers and the encoder were acquired digitally by an IOTEC analogue-to-digital converter with a sampling rate of 10 000 samples s^{-1} during the deployment of the actuator. Analogue low-pass filtering of the incoming signals was carried out before digitization with a cutoff frequency set at 500 Hz. Control of the actuator motion and the data acquisition was provided in a Matlab program written for synchronizing these two processes.

The aerodynamic balance and deployment mechanism system used in the present experiments, along with the data acquisition system were specifically designed, tested and fine-tuned to carry out high-speed deployment of the actuator, measure relatively low-magnitude force and acquire data that could be interpreted without any filtering. Inevitably though, electronic noise and mechanical vibrations at the natural frequency of the system were present in some of the experiments and filtering was applied during the data processing phase of our investigation.

The filter used for all of the experiments was a second-order, low-pass, Type I, Chebyshev filter with 0.1 dB of ripple in the pass band, a cutoff frequency of 10 Hz and of minimal phase shift. These filtering parameters were established after a systematic process in which the physics of the experiment, the effects of decreasing cutoff frequency and the timing of events were carefully considered. To illustrate the effects of filtering, the raw output data of the encoder, presented in figure 3(*a*), are compared with the corresponding filtered data. No substantial phase shift can observed between the two signals. Owing to the high-inertia forces generated during high-rotational-speed experiments, the servo-motor cannot abruptly stop the actuator at exactly 90°, while keeping up the high rotational speed all of the way to the end. In order to avoid a large overshoot and to ensure the actuator stops at 90°, a hard stop with a rubber dampener is introduced at that point. The overshoot is therefore restricted, but when the actuator hits the hard limiter, the abrupt stop produces high-frequency vibrations of many modes. These vibrations are recorded by the data acquisition system, but they are aerodynamically irrelevant to our experiments and their spectral content is in frequencies higher that the frequencies of interest of the present flow. Figure 3(*b*) shows the raw and filtered signals output signal of the load cell measuring the lift component of the force obtained at one of the highest deployment rates. As shown in figure 3(*a*), the angular location of 90° in this experiment is reached at approximately 0.77 s. As in the case of the encoder data, the filtered and unfiltered data for the lift signal up to 90° are highly correlated. The two correlation coefficients computed are 0.999 for the data in figure 3(*a*) and 0.957 for the data in figure 3(*b*). When the hard stop is hit at approximately 0.77 s, the lift load cell, as shown in figure 3(*b*), records various modes of damped mechanical vibrations from the entire apparatus which are of no interest to the present experiment. The amplitude of these oscillations is substantially reduced in the filtered lift signal which drops to zero value for times beyond the 90° angular location.

4. Actuator kinematics and inertia effects

In the following a stationary coordinate system located on the wall of the wind tunnel is assumed and a polar coordinate system is used to describe the motion of the rotating actuator with definitions of various parameters as shown in figure 4. The

(a)

Filtered versus unfiltered angle

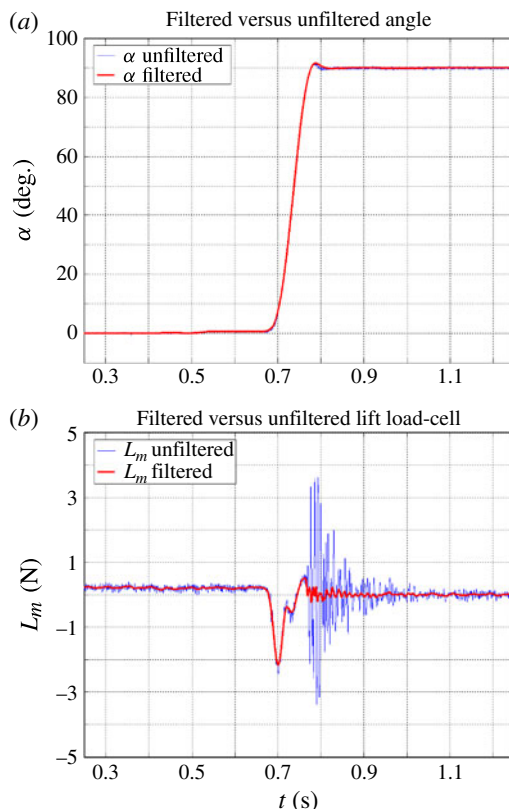(b)

Filtered versus unfiltered lift load-cell

FIGURE 3. (Colour online) (a) Encoder raw (unfiltered) data (shown in blue online) and filtered data (shown in red online). Square actuator, $Str = 0.21$, $U_0 = 11$ m s^{-1}. (b) Lift raw (unfiltered) data (shown in blue online) and lift filtered data (shown in blue online). Square actuator, $Str = 0.21$, $U_0 = 11$ m s^{-1}.
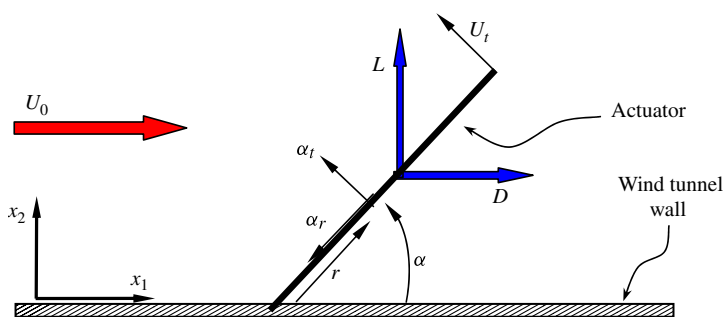

FIGURE 4. (Colour online) Stationary coordinate system on wind tunnel wall and polar coordinate system for a moving actuator; a_t = tangential acceleration, a_r = radial acceleration, α = angle, U_t = tip velocity and U_0 = free stream velocity.

time-dependent angular location of the actuator during deployments at various velocity ratios *Str* is shown in figure 5(a). In these experiments, the initial deployment angle is $\alpha_i = 0°$ and the final angle $\alpha_f = 90°$. Since the angular velocity which controls
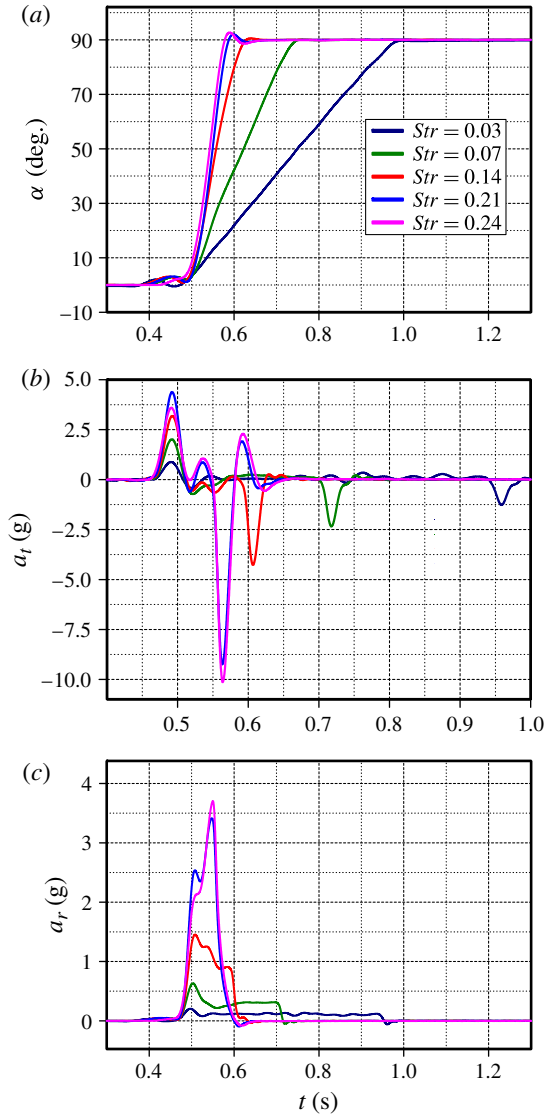
FIGURE 5. (Colour online) (*a*) Angular location of an actuator during its deployment for various dimensionless angular velocities. Square actuator, $\alpha_f = 90°$, $U_0 = 10.69$ m s^{-1} and $d = 5$ cm. (*b*) Tangential acceleration of an actuator during its deployment for various dimensionless angular velocities. Square actuator, $\alpha_f = 90°$, $U_0 = 10.69$ m s^{-1} and $d = 5$ cm. (*c*) Radial acceleration of an actuator during its deployment for various dimensionless angular velocities. Square actuator, $\alpha_f = 90°$, $U_0 = 10.69$ m s^{-1} and $d = 5$ cm.

the deployment rate is defined as $\omega = \partial\alpha/\partial t$ the data show that the duration of the deployment between fixed angles α_i and α_f is extended with decreasing *Str*.

The time-dependent measurements of the tangential acceleration $a_t = (\partial\omega/\partial t)r$ relative to the gravitational acceleration g are shown in the figure 5(*b*). They have been obtained directly from the accelerometer output since differentiating the data shown in figure 6(*a*) twice requires higher temporal resolution than that available in the current
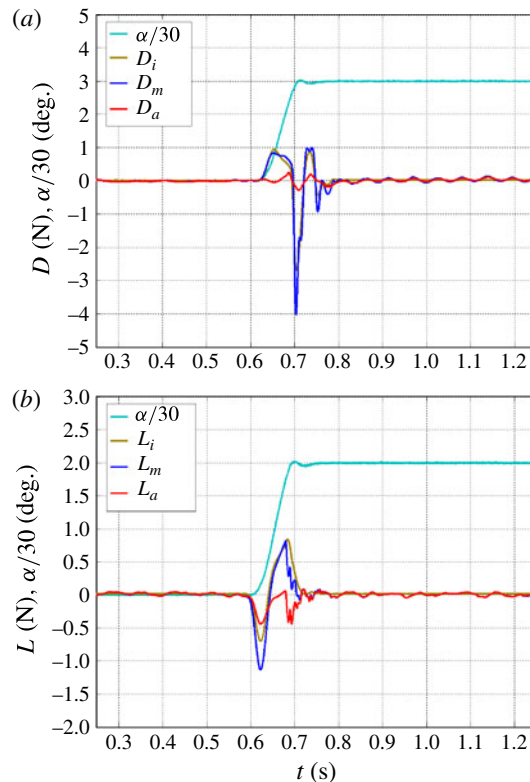
FIGURE 6. (Colour online) (*a*) Comparison of directly measured drag D_m, inertia force in the drag direction D_i and resultant aerodynamic drag force D_a in an experiment without airflow, with 10 cm × 10 cm square winglet, $\omega = 22$ rad s^{-1} and $\alpha_f = 90°$. (*b*) Comparison of directly measured lift L_m, inertia force in the lift direction L_i and resultant aerodynamic lift force L_a in an experiment without airflow, with 10 cm × 10 cm square winglet, $\omega = 22$ rad s^{-1} and $\alpha_f = 90°$.

encoder. For *Str* lower than 0.14, the data in figure 5(*b*) show that the motion of the actuator is characterized by acceleration initially which is followed by constant angular velocity motion with zero tangential acceleration and a final decelerating period before it stops. In the high *Str* cases, there is no constant velocity zone and the initial and final periods associated with acceleration and deceleration respectively are blended together.

The corresponding radial acceleration data $a_r = \omega^2 r$ are shown in figure 5(*c*). Radial acceleration does not change sign during the deployment about the same axis of rotation and is always pointing towards the centre of rotation. At lower *Str*, a_r reaches a certain level and remains constant for some time before it drops to zero. At high *Str*, there is no real constant acceleration period and the initial onset of acceleration overlaps with its removal.

The measured forces have been compensated for by the effects of inertia of the actuator itself which have been determined by using the acceleration information. The so-calculated inertia forces were compared directly with the forces measured by the load cells without airflow in the wind tunnel. Under these circumstances, most of the force measured is due to inertia, the resistance of air during the motion and the low
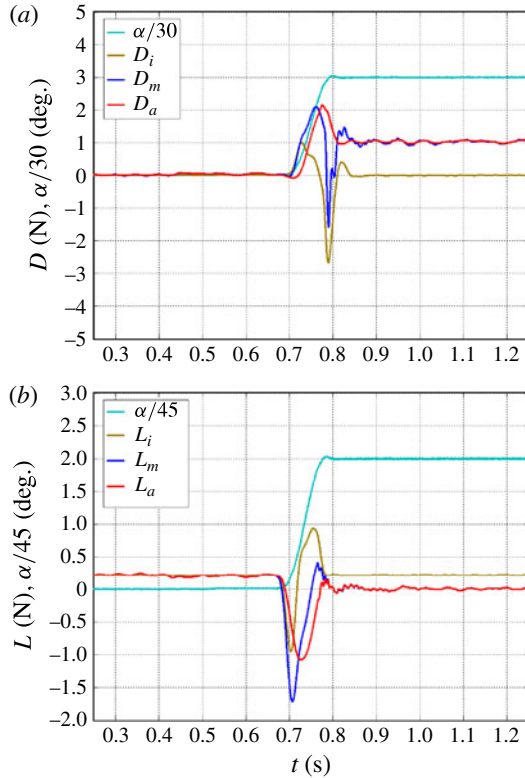
FIGURE 7. (Colour online) (*a*) Inertia, measured and resultant aerodynamic drag forces in an experiment with airflow, with 10 cm × 10 cm square actuator, $\omega = 22$ rad s^{-1} and $\alpha_f = 90°$. (*b*) Inertia, measured and resultant aerodynamic lift forces in an experiment with airflow, with 10 cm × 10 cm Square actuator, $\omega = 22$ rad s^{-1} and $\alpha_f = 90°$.

pressure created by the departing actuator. Measurements obtained with no air flow have been compared with the directly measured drag by the load cell D_m and the inertia force in the drag direction D_i as shown in figure 6(*a*). Their difference is the true aerodynamic force D_a which in comparison with the maximum values of D_m or D_i is very small, practically close to zero. In figure 6(*b*) there is, however, some small quantitative difference between the inertia calculated lift force L_i and the measured force L_m during the early stages of deployment. This difference is most probably due to the low pressure created during the sudden lifting of the actuator from its small cavity on the wall, which generates a downward force with a component in the lift direction.

The above tests showed that the inertia forces during the actuator deployment can be accurately estimated by using the acceleration data. This enables us to subtract the inertia effects from the measured force data and obtain the actual lift and drag forces. Figure 7(*a*,*b*) show how the process of eliminating inertia effects is applied to the measured data of drag and lift to obtain D_a and L_a in an experiment with air flow. The D_m data shown in figure 7(*a*) show that the drag is positive in the beginning of the deployment and it increases with the time, i.e. the deployment angle for up to about 60° and then it is suddenly reduced to negative values due to the large deceleration during the last stages of the deployment. The inertia force D_i follows the drag D_m
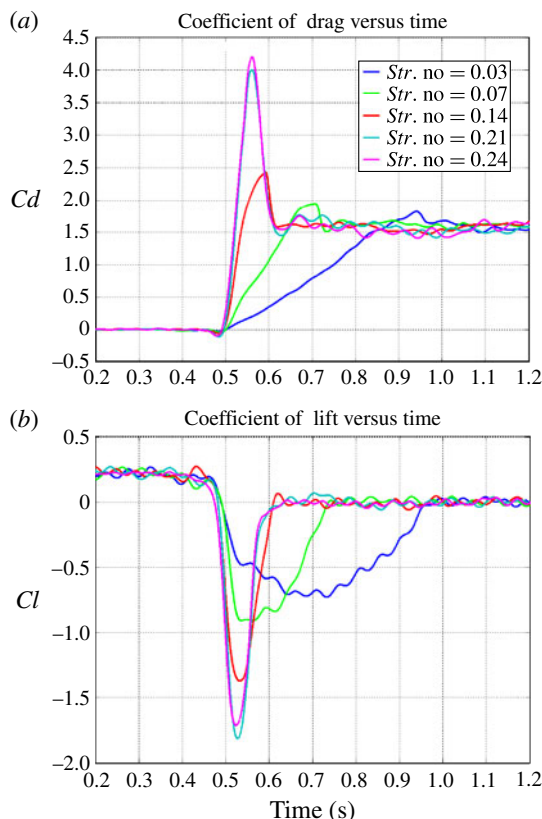
(*a*)

Coefficient of drag versus time

Str. no = 0.03	
Str. no = 0.07	
Str. no = 0.14	
Str. no = 0.21	
Str. no = 0.24	

(*b*)

Coefficient of lift versus time

Time (s)

FIGURE 8. (Colour online) Angular velocity effects on dynamic drag coefficient. Deployment angle from 0 to 90°, $U_0 = 10.69$ m s^{-1}, boundary layer thickness $\delta = 5$ cm, square panels. (*b*) Angular velocity effects on dynamic lift coefficient. Deployment angle from 0 to 90°, $U_0 = 10.69$ m s^{-1}, boundary layer thickness $\delta = 5$ cm, square panels.

very early in the deployment but these two quantities depart from each other at higher angles. The net aerodynamic drag D_a increases quickly with the angle and at the end reverts to a steady state with a constant value. It is of interest to observe that the maximum (absolute) value of the lift L_a takes place at about $\alpha = 40°$ while the maximum drag D_a occurs much later in the deployment at about $\alpha = 80°$ while shortly after the end of deployment both reach their steady-state values. Thus, the dynamic deployment and the associate transient flow conditions not only increase the forces but also delay the onset of steady state in a nonlinear way.

5. The effects of angular velocity

Several experiments were carried out to establish the effects of the actuator deployment speed on the development of forces while keeping the incoming free stream flow velocity U_0 constant. Velocity ratios from $Str = 0.03$ to 0.24 were achieved in these experiments. These effects are demonstrated in figure 8(*a*,*b*) where the force coefficients $Cd = D_a/(A\rho U_0^2/2)$ and $Cl = L_a/(A\rho U_0^2/2)$ are plotted as a function of time for various experiments at constant free stream velocity U_0 and different angular velocities of the actuator deployment ω. Here A is the planform area of the actuator defined in the present case as $A = b \cdot h$. The deployment is always at

constant angular speed ω except at the beginning and at the end of the travel time and therefore the time is proportional to the angular position of the actuator α since $\alpha = \omega t$.

The lowest *Str* case can be considered as a quasi-steady-state experiment, since the deployment velocity is slow compared with the free stream velocity. The drag coefficient simply increases to the steady state with a small overshoot at the end of the deployment. As the *Str* and deployment speed increase, apparent by the steeper and steeper angles at which drag is increasing with time, the maximum dynamic drag exerted on the panel is also increased. As the drag force coefficient increases with increasing deployment angle α it reaches its maximum value at about 80°. The ratio of the maximum dynamic drag force to that of the static force appears to increase with increasing ω, i.e. with increasing *Str* number which expresses the ratio U_r/U_0. Thus, the greater the relative velocity of the actuator tip, the greater is the ratio of the forces and therefore the dynamic deployment effect. The data also demonstrate that the peak dynamic *Cd* is always greater than the static aerodynamic force coefficient, suggesting a surplus of control force during dynamic operation of the flaps.

Of equal importance to the drag is the effect that the increasing deployment speed has on the coefficient of lift. Figure 8(*b*) shows the coefficient of lift *Cl* with respect to time for the same set of experiments, as the deployment speed for the panel increases from 3 to 26 rad s^{-1}. Figure 8(*b*) shows that the lift development with respect to the deployment angle is qualitatively different than that of the drag. It has a negative peak which increases in absolute value with increasing *Str* and occurs at much earlier deployment times/angles. At the end of the deployment reaches zero values in all cases and the dc offset observed before deployment is due to the pressure difference which exists between the working section wall and the ambient.

6. The effects of final angle deployment

In another set of experiments the final deployment angle, α_f, was varied and the lift and drag forces were measured while keeping the velocity ratio constant. This behaviour was investigated for deployment angles ranging from 0 to 15, 30, 45, 60, 75 and 90°. Each of these experiments was carried out at a constant velocity ratio 0.24. Figure 9(*a*) shows the effect of final deployment angle on dynamic and static drag coefficient. This figure differs from figure 8(*a*) in several ways. In figure 8(*a*), the rate of rise of drag with time is almost the same, as expected, since all experiments were conducted at the same Strouhal number. In figure 9(*a*) the rising slope of drag is different for every experiment, since the experiments were performed with different velocity ratios and therefore different deployment speeds. Another fundamental difference is that in figure 9(*a*) the steady-state drag is not the same at the end of each dynamic state as expected, since the steady-state angle α_f is different for every experiment. This is not the case in figure 8(*a*), since the final deployment angles were all equal to 90°. As can be seen in figure 8(*a*), there is a significant increase in drag during the dynamic phase of these experiments. Figure 9(*b*) shows the lift coefficient as a function of time for deployments of different durations. The maximum dynamic effect in absolute sense increases with the increasing angle α_f. Just as in the case of the drag coefficient, the steady-state lift coefficient for different final deployment angles exhibits a different behaviour. A significant qualitative difference between figure 9(*a*,*b*) is that the maximum dynamic drag coefficient has a clear monotonic increase with increasing deployment angle. In the case of lift, this is not as clear. The dynamic lift coefficient has a more complex
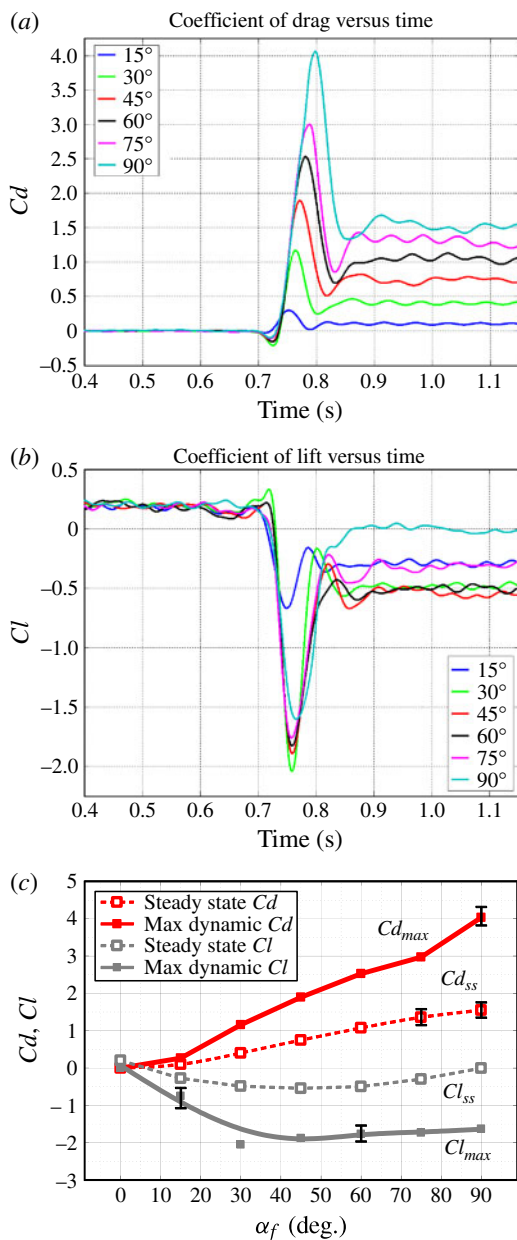
FIGURE 9. (Colour online) Effect of varying final deployment angle on drag coefficient. Square actuator, $Str = 0.24$, $U_0 = 10.69\ \text{m s}^{-1}$, 5 cm boundary layer. (b) Effect of varying final deployment angle on lift coefficient. Square actuator, $Str = 0.24$, $U_0 = 10.69\ \text{m s}^{-1}$, 5 cm boundary layer. (c) Steady-state and maximum dynamic force coefficients during experiments with various final deployment angles. Case of square actuators in the $\delta = 5$ cm thick boundary layer.

behaviour than the drag coefficient for the same conditions. At the end of the dynamic effect the lift coefficients revert to their steady-state values which are not zero.

Figure 9(c) shows the steady-state values of the drag and lift coefficients, Cd_{ss} and Cl_{ss}, respectively, measured at each experiment with different final angle of

deployment α_f together with their maximum values obtained in the corresponding dynamic deployments. The steady state values of Cd increase with α_f and reach a maximum value of $Cd = 1.49$ at $\alpha_f = 90°$ as expected. This value is smaller than that measured in the free steam of the wind tunnel because of the wall presence as was found in a companion experiment aimed to determine the steady state values of Cd of low-aspect-ratio flat plates normal to the flow at various distances from the wall. The maximum dynamic Cd_{max} also increases with α_f and actually occurs at angles slightly smaller than $\alpha < \alpha_f$. There is always a gain in the drag coefficient due to dynamic effects expressed as $\Delta Cd_m = Cd_{max} - Cd_{ss}$ which increases with α_f and reaches a maximum of $\Delta Cd_m = 2.5$ at $\alpha_f = 90°$. The steady-state lift coefficient starts with a slightly positive value at $\alpha_f = 0$ due to the static pressure difference across the wind tunnel wall and increases in absolute sense with α_f up to 50° before it decreases to smaller values eventually reaching a zero value at $\alpha_f = 90$. The maximum value of the dynamic lift coefficient Cl_{max} increases with α_f up to about 40° and maintains a practically constant value of 1.55 after 60°.

7. The effect of actuator planform geometry

A comparison of the aerodynamic lift and drag coefficients for the two shapes of actuators investigated here is shown in figure 10(*a*). It appears that the drag coefficient during the dynamic deployment of the square flap is always higher than that of the triangular shape suggesting that delta-wing shapes are aerodynamically less efficient than squares. The lift coefficient for the square shape is also slightly larger in absolute terms than the corresponding triangular shape actuator. A direct comparison between the values of Cd_{max} and Cl_{max} of the two different planforms obtained as a function of Str is shown in figure 10(*b*). A strong dependence of Cd_{max} and Cl_{max} of both planforms on Str is evident from these data with the values of the triangular actuators being always smaller than the corresponding values of the square actuators. It also appears that the difference in the force coefficients between these two shapes increases with Str.

The experiments also showed higher forces in the case of the square flaps than forces obtained in the delta wing case. This is mostly due to the fact that the area of the square flap is twice as large as that of the delta wing. Thus, the controlling forces generated by the square shape flaps are higher in magnitude as well as in non-dimensional terms than the forces generated by the triangular ones.

8. The effect of incoming boundary layer

One key parameter describing the effect of the incoming boundary layer on the aerodynamic performance of these control surfaces, to first order, is its Reynolds number based on the momentum thickness Re_θ. This Reynolds number and Re_h constitute two independent parameters of the present flow. Their ratio Re_h/Re_θ is proportional to the ratio of the height of the actuator h to the boundary layer thickness δ, i.e. $Re_h/Re_\theta = h/\theta \sim h/\delta$. Thus, by considering the influence of h/δ effectively we are addressing the effects of Re_θ on the aerodynamic performance of the actuators for a fixed Re_h.

Two flow cases have been investigated experimentally: one with $h/\delta = 0.71$ and a second one with $h/\delta = 2$. This was achieved by setting up the actuator at two different longitudinal locations in the working section under practically the same $Re_h = hU_0/\nu$. In the first case, the actuator with the balance was installed at $x_1 = 6$ m from the beginning of the working section and in the second case it was moved upstream
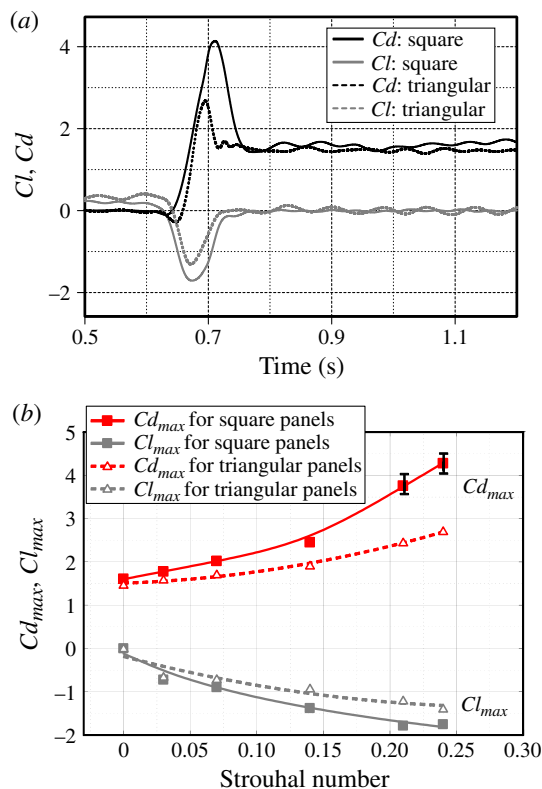
FIGURE 10. (Colour online) (*a*) Lift and drag coefficients for square and triangular actuators at $Str = 0.24$ and $h/\delta = 2$. (*b*) Effects of Str on maximum dynamic force coefficients Cd and Cl for the square and triangular planform actuators embedded in the $\delta = 14$ cm thick boundary layer.

to $x_1 = 2$ m. In both cases, the free stream velocity was maintained at about the same value. The flow parameters of the experiments carried out in these two locations are listed in table 1.

A typical comparison between the data obtained at these two different locations is shown in figure 11(*a*) where the results obtained for the lift and drag coefficients are plotted as a function of time. The drag data are systematically higher in the case of $h/\delta = 2$ than in the case of $h/\delta = 0.71$ and at the peak of the dynamic effects they are up to 40 % greater. The peak lift coefficient is also slightly greater in the case of the thinner boundary layer with $h/\delta = 2.0$. The values of maximum force coefficients during the dynamic deployment are plotted in figure 11(*b*) against Str for the two cases of h/δ. The increase in Str has a dramatic effect on the maximum value of the drag coefficient which increases substantially. The data of the $h/\delta = 2$ case show clearly higher values than the corresponding $h/\delta = 0.71$ data for the same Str. In addition, the rate of increase of Cd_{max} with Str is higher in the thinner boundary layer with $h/\delta = 2$. Similar is the qualitative and quantitative behaviour of the triangular actuators embedded in the two different boundary layers.

The data shown in figure 11(*a,b*) as well the rest of the experimental data obtained in the present investigation show that the deeper the actuators are embedded in the
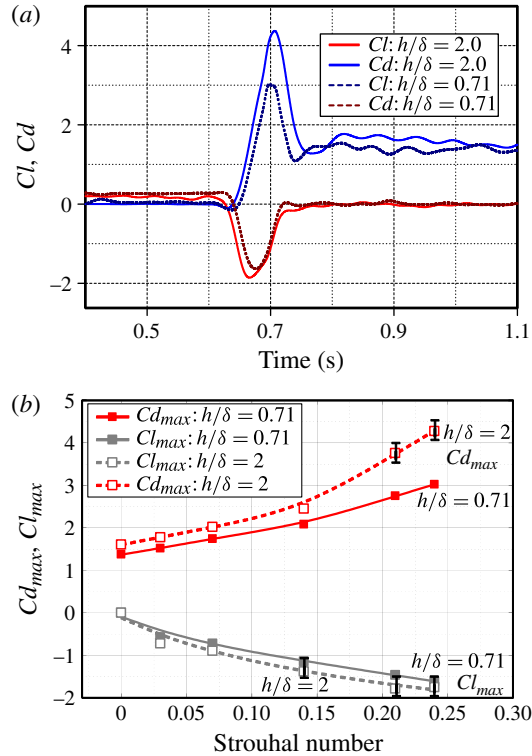
FIGURE 11. (Colour online) (*a*) Effect of boundary layer thickness on force generation. Case of square actuators with $Str = 0.24$. (*b*) Effect of boundary layer thickness on force coefficients in the case of square actuators. Open symbols, $h/\delta = 2$; filled symbols, $h/\delta = 0.71$.

boundary layer the lower the forces and their coefficients. In order to explain this behaviour, we first explored the possibility that this effect is due to the difference in the incoming fluid momentum which the actuator experiences between the two boundary layers investigated. An effective mean velocity based on an area-averaged velocity across the boundary layer $\overline{U}_{eff} = (1/A) \int_0^h \cdot^b U \, \mathrm{d}A$ was estimated for the two cases under the assumption of an exponential variation of the U with the distance from the wall, i.e. $U/U_0 = (x_2/\delta)^n$ with $n = 1/7$. These estimates showed a ratio of the two effective velocities $\overline{U}_{eff2}/\overline{U}_{eff1} = 1.04$ where the indices 1 and 2 refer to the $h/\delta = 2$ and 0.7 cases, respectively. This effect would make the corresponding ratio of $Cd_{max2}/Cd_{max1} = (1.04)^2 = 1.08$. The experimental data shown in figure 10(*b*), however, indicate a range of this ratio from 1.12 at $Str = 0$ to 1.41 at $Str = 0.23$. Thus, this effect accounts for only a small portion of the difference in the Cd_{max} data between the two boundary layers. Additional consideration of Str effects reduces slightly more this difference. The ratio Str expresses the ratio of two velocities U_r/U_0 where U_0 has the role of $\overline{U}_{eff}$. For actuators with $h \ll \delta$, the effective free stream velocity $\overline{U}_{eff}$ which is the velocity of the upstream flow seen or felt by the actuator, is smaller than U_0 and therefore the effective velocity ratio Str is slightly higher than the nominal one. As a result of the small relative difference in Str for the same rotational speed, dynamic effects are expected to be slightly stronger in the case of thicker boundary layers.
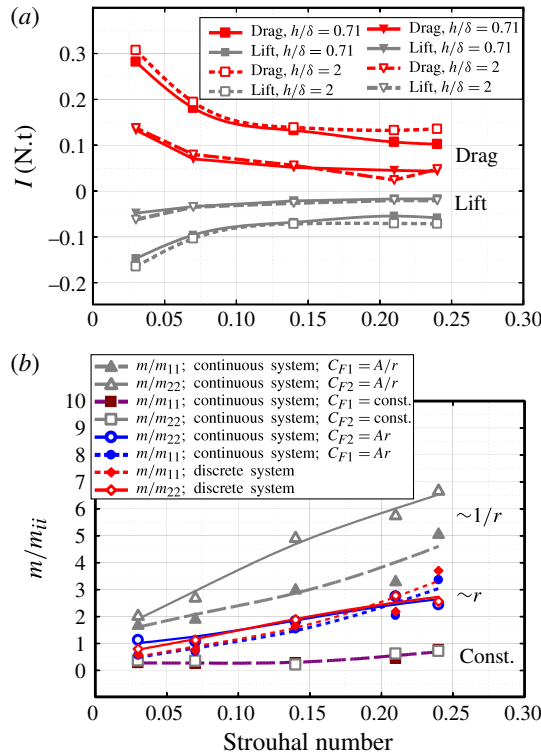
FIGURE 12. (Colour online) (*a*) Impulse of drag and lift forces at various *Str* for the two different planforms and two different h/δ. Symbols: ■, square actuators; ▼, triangular actuators. Open symbols, $h/\delta = 2$; filled symbols, $h/\delta = 0.71$. (*b*) Added mass effects m/m_a at various *Str* in the case of square actuators with $h/\delta = 0.71$ according to continuous and discrete models.

However, this increase is not significant and it cannot entirely explain the difference in Cd_{max} between the two boundary layer cases. Additional dynamic effects related to the formation of large-scale vortical structures offer a more plausible explanation of this behaviour.

9. Impulse of drag and lift forces

Newton's second law can be applied to estimate the impulse of the lift and drag forces during the deployment of the actuators between 0 and t_1 times

$$I = \int_0^{t_1} \boldsymbol{F}\, \mathrm{d}t = \int_0^{t_1} \mathrm{d}m\boldsymbol{V} = \int_0^{t_1} m\boldsymbol{V}. \tag{9.1}$$

Thus, an integration of the time-dependent drag and lift forces over time can provide an estimate of the momentum changes caused by the deployment of the actuators. The impulse relation (9.1) can be extended to provide an estimate of the overall energy the motor has to expend, in order to create the deployment effect desired for every experiment.

Figure 12 shows the impulse of drag and lift forces at various *Str* for the experiments involving the two planforms of the actuators embedded in two boundary

layers of different thickness. An interesting observation stemming from the data in this figure is that the impulse needed for the deployment of the actuators is reduced with increasing *Str* at higher deployment speeds. This is a significant result, since it shows that while attaining higher drag and lift forces by as much as 200%, the momentum input to the flow is reduced by 70%. The reason for this behaviour is that the time duration of each deployment $\Delta t_1 = t_1 - 0$ diminishes much faster with *Str* than the increase in the force. The duration Δt_1 is inversely proportional to ω which varies from the slowest to the fast experiment by a factor of 8.5 while the corresponding force increases by at most a factor of 2–3. Thus, the overall momentum addition to the flow ends up being less at higher deployment velocities.

Further insight into this behaviour can be obtained by considering the dynamic equation governing the motion of the panel

$$m\ddot{x}_i + c\dot{x}_i + kx_i = F_i + F_{i,drive} \tag{9.2}$$

where m is the mass of the system, c is its damping coefficient and k its stiffness. Here F_i is the aerodynamic force acting on the panel in the x_i direction ($i = 1, 2$), F_{drive} is the force provided by the drive mechanism and $\ddot{x}_i$, $\dot{x}_i$ and x_i are the acceleration, velocity and displacement of the centre of mass, respectively, in the i direction. The force F_i can be decomposed into added mass and added damping terms (see Vikestad, Vandiver & Larsen 2000) as

$$F_i = -m_{ii}\ddot{x}_i - c_{ii}\dot{x}_i. \tag{9.3}$$

The added mass term m_{ii} and the added damping coefficient c_{ii} can be estimated from this equation by multiplying it by $\dot{x}_i$ or $\dot{x}_i$ and time-averaging to yield

$$m_{ii} = \frac{\int_0^{t_1} F_i \ddot{x}_i \, \mathrm{d}t}{\int_0^{t_1} \ddot{x}_i \ddot{x}_i \, \mathrm{d}t} \quad \text{and} \quad c_{ii} = \frac{\int_0^{t_1} F_i \dot{x}_i \, \mathrm{d}t}{\int_0^{t_1} \dot{x}_1 \dot{x}_1 \, \mathrm{d}t}, \tag{9.4}$$

respectively. These coefficients have been computed from the experimental data, first according to the discrete or lumped parameter model and second according to the distributed parameter or continuous model. In the first approach, the mass of the panel is lumped at its centre where also the aerodynamic forces act. In the second approach, the aerodynamic forces are continuously distributed over the panel and the derivation of the resultant force is based on blade element theory. An infinitesimally small area/strip ($b\,\mathrm{d}r$) on the panel/blade moving with tangential velocity (ωr) and subjected to an upstream mean velocity $U(x_2)$ inside the boundary layer has a relative velocity in the normal direction to the surface of the panel $\omega r + U(x_2) \sin\alpha$. The local normal force is modelled through

$$\mathrm{d}F_N(r, t) = p(r, t)b\,\mathrm{d}r = C_N(r, t)1/2\rho\left[\omega r + U(x_2)\sin\alpha\right]^2 b\,\mathrm{d}r \tag{9.5}$$

where $p(r, t)$ is the pressure acting on the panel, $C_N(r, t)$ is the local normal force coefficient and $Str(r/h)$ is the local Strouhal number $Strl = \omega r/U_0$. The velocity $U(x_2)$ can be estimated from $U(x_2) = U_0 (x_2/\delta)^n$ with $n = 1/7$ and $x_2 = r\sin\alpha$. The above relation leads to

$$\mathrm{d}F_N(r, t) = p(r, t)b\,\mathrm{d}r = C_N(r, t)1/2\rho U_0^2\left[Str\frac{r}{h} + \left(\frac{r\sin\alpha}{\delta}\right)^n \sin\alpha\right]^2 b\,\mathrm{d}r. \tag{9.6}$$

Let us define

$$\mathscr{F}(r, t) = \left[Str\frac{r}{h} + \left(\frac{r \sin \alpha}{\delta} \right)^n \sin \alpha \right]^2$$

$$= \left[Str^2 \left(\frac{r}{h} \right)^2 + 2Str\frac{r}{h} \left(\frac{r \sin \alpha}{\delta} \right)^n \sin \alpha + \left(\frac{r \sin \alpha}{\delta} \right)^{2n} \sin^2 \alpha \right]. \quad (9.7)$$

It is very instructive to assume a given distribution for $C_N(r, t)$ and consider its effect on the force F_N. Our computational fluid dynamics (CFD) work (Pierides 2011) has indicated that the pressure over the actuator during deployment is uniform initially and then an overpressure is developed towards its tip. This pressure distribution can be approximated by a quadratic equation in terms of r in all regions except near the edges of the panel while the quantity $\mathscr{F}(r, t)$ varies as $\sim r^2$. Practically, however, since the coefficient $Str^2 = (0.3)^2$ is small, the quadratic term $Str^2 (r/h)^2$ may be neglected in comparison with the other terms and therefore $\mathscr{F}(r, t)$ varies as r. Matching the requirements for the two distributions of $p(r, t)$ and $\mathscr{F}(r, t)$ leads to a linear variation of $C_N(r, t)$ with r as the only compatible possibility. Thus, a linear variation with slope $dC_N(r, t)/dr = C_N(h, t)/h$ is adopted with $C_N(0, t) = 0$.

The normal force can be decomposed into two components along the drag and lift directions x_1 and x_2:

$$dF_1(r, t) = C_N(r, t) \sin a1/2\rho \left[\omega r + U(x_2) \sin \alpha \right]^2 b \, dr \quad (9.8)$$

$$dF_2(r, t) = C_N(r, t) \cos a1/2\rho \left[\omega r + U(x_2) \sin \alpha \right]^2 b \, dr. \quad (9.9)$$

The concept of distributed added mass m_{ii} assumes that an infinitesimally small aerodynamic force dF_i acting on a $b \, dr$ strip will cause an acceleration in the nearby fluid $\ddot{x}_i$ of a mass dm_{ii} so that $dF_i = \ddot{x}_i \, dm_{ii}$ where $dm_{ii} = \rho b s \, dr$ with s the thickness of the layer with the added mass.

If we multiply by $\ddot{x}_i$ both sides we obtain

$$\ddot{x}_i \, dF_i = \ddot{x}_i \ddot{x}_i \, dm_{ii}. \quad (9.10)$$

The acceleration is $\ddot{x}_i = A_i r$ with $A_1 = (\omega^2 \cos \alpha + \partial \omega / \partial t \sin \alpha)$ and $A_2 = (-\omega^2 \sin \alpha + \partial \omega / \partial t \cos \alpha)$. If we integrate the previous equation we can obtain

$$\int_0^h \ddot{x}_i \, dF_i = \int_0^h \ddot{x}_i \ddot{x}_i \, dm_{ii} = A_i A_i \int_0^h r^2 \rho b s \, dr$$

$$= \frac{1}{3} \ddot{x}_i(h, t) \ddot{x}_i(h, t) m_{ii} = \frac{4}{3} \ddot{x}_i \left(\frac{h}{2}, t \right) \ddot{x}_i \left(\frac{h}{2}, t \right) m_{ii} \quad (9.11)$$

where $\ddot{x}_i(h/2, t)$ is the acceleration at the centre of mass. This leads to the definition of m_{ii} according to the distributed parameter model as

$$m_{ii} = \frac{\displaystyle\int_0^{t_1} \int_0^h \ddot{x}_i \, dF_i \, dt}{\displaystyle\frac{4}{3} \int_0^{t_1} \ddot{x}_i \left(\frac{h}{2}, t \right) \ddot{x}_i \left(\frac{h}{2}, t \right) dt}. \quad (9.12)$$

It appears that

$$\int_0^h \ddot{x}_i \, \mathrm{d}F_i = 2F_i \ddot{x}_i \left(\frac{h}{2}, t \right)$$

$$\times \frac{\left[\dfrac{1}{5} Str^2 + 2Str \dfrac{1}{n+4} \left(\dfrac{h \sin \alpha}{\delta} \right)^n \sin \alpha + \dfrac{1}{2n+3} \left(\dfrac{h \sin \alpha}{\delta} \right)^{2n} \sin^2 \alpha \right]}{\left[\dfrac{1}{4} Str^2 + 2Str \dfrac{1}{n+3} \left(\dfrac{h \sin \alpha}{\delta} \right)^n \sin \alpha + \dfrac{1}{2n+2} \left(\dfrac{h \sin \alpha}{\delta} \right)^{2n} \sin^2 \alpha \right]} \quad (9.13)$$

where $\alpha = \omega t$.

These relations are introduced into (9.12) and after integration over time the coefficients are obtained for each of the two models. Two additional cases with different pressure distributions on the panel have been also investigated according to the distributed parameter theory. In the first case, a constant pressure distribution on the moving panel is assumed which requires C_N to vary as $\sim r^{-1}$. In the second case, a trapezoidal distribution is assumed with C_N considered independent of r.

The integral $(4/3) \int_0^{t_1} \ddot{x}_i(h/2, t) \, \dot{x}_i(h/2, t) \, \mathrm{d}t$ is the same in all three cases while the integral $\int_0^{t_1} \int_0^h \ddot{x}_i \, \mathrm{d}F_i \, \mathrm{d}t$ differs only in the coefficients of the terms inside the brackets.

$$\int_0^h \ddot{x}_i \, \mathrm{d}F_i = 2F_i \ddot{x}_i \left(\frac{h}{2}, t \right)$$

$$\times \frac{\left[\dfrac{1}{3} Str^2 + 2Str \dfrac{1}{n+2} \left(\dfrac{h \sin \alpha}{\delta} \right)^n \sin \alpha + \dfrac{1}{2n+1} \left(\dfrac{h \sin \alpha}{\delta} \right)^{2n} \sin^2 \alpha \right]}{\left[\dfrac{1}{2} Str^2 + 2Str \dfrac{1}{n+1} \left(\dfrac{h \sin \alpha}{\delta} \right)^n \sin \alpha + \dfrac{1}{2n} \left(\dfrac{h \sin \alpha}{\delta} \right)^{2n} \sin^2 \alpha \right]} \quad (9.14)$$

and

$$\int_0^h \ddot{x}_i \, \mathrm{d}F_i = 2F_i \ddot{x}_i \left(\frac{h}{2}, t \right)$$

$$\times \frac{\left[\dfrac{1}{4} Str^2 + 2Str \dfrac{1}{n+3} \left(\dfrac{h \sin \alpha}{\delta} \right)^n \sin \alpha + \dfrac{1}{2n+2} \left(\dfrac{h \sin \alpha}{\delta} \right)^{2n} \sin^2 \alpha \right]}{\left[\dfrac{1}{3} Str^2 + 2Str \dfrac{1}{n+2} \left(\dfrac{h \sin \alpha}{\delta} \right)^n \sin \alpha + \dfrac{1}{2n+1} \left(\dfrac{h \sin \alpha}{\delta} \right)^{2n} \sin^2 \alpha \right]} \quad (9.15)$$

for the constant and trapezoidal pressure distributions, respectively.

The results computed in these three cases together with the results obtained with the lumped parameter theory are shown in figure 12(b).

Qualitatively, the data of m/m_{ii} from both models and in all cases of pressure distributions considered here increase with Str. This trend appears to be independent of the assumed distribution of the force coefficients. To a very good approximation, the data in this figure seem to increase linearly with Str. In fact, this trend is expected because $\ddot{x}_i \sim Str$, $F_i \sim (1 + Str)^2$ and therefore

$$\frac{1}{m_{ii}} \sim \frac{\ddot{x}_i}{F_i} \sim \frac{Str}{(1 + Str)^2} \approx Str \, (1 - 2Str) \approx Str - 2Str^2 \approx Str. \quad (9.16)$$

There is considerable difference, however, among the various cases developed under the continuous system approach and the three different distributions of force coefficients along the panel. During one duty cycle of the panel's deployment, the pressure is initially constant along the radial distance r (i.e. $C_F \sim 1/r$) then becomes trapezoidal (i.e. $C_F \sim$ const) and eventually develops an overpressure towards its tip which can be approximately expressed by a quadratic distribution (i.e. $C_F \sim r$). The added mass data are the results of integration over the complete cycle of the deployment and it is expected they include contributions from all of these three different pressure/force coefficient distributions. The data shown above in which m_{ii} have been computed under the assumption of $C_F \sim 1/r$ or $C_F =$ constant through the whole cycle are unrealistic and do not represent the most basic features of the deployment physics. The quadratic pressure distribution with a linear distribution of the force coefficients appears to be a better approximation of the processes since it can describe reasonably well the early phases of deployment with constant or trapezoidal pressure distributions and more accurately the later stages when the vortex structure creates the over pressure at the tip.

It is also interesting to note that the results of the lumped-mass system approach are very close to those obtained under the continuous system assumption with linear distribution of C_F. Thus, a less complex model described by single-degree-of-freedom equations that are relatively simple to solve analytically appears to perform equally well with the more sophisticated continuous system model.

If the impulse of (9.3) $I = I_{mii} + I_{cii}$ is introduced in to the impulse of (9.2) the following relation can be obtained:

$$\frac{I_m}{I} + \frac{I_c}{I} + \frac{I_k}{I} = 1 + \frac{I_{drive}}{I}. \tag{9.17}$$

The factor $1/I$ can be further expanded as $1/I = 1/(I_{mii} + I_{cii}) \approx 1/I_{mii} - I_{cii}/I_{mii}^2 \approx 1/I_{mii}$ for $I_{cii} \ll I_{mii}^2$. Then (9.17) can be transformed into

$$\frac{m}{m_{ii}} + \frac{I_c}{I} + \frac{I_k}{I} = 1 + \frac{I_{drive}}{I}. \tag{9.18}$$

The estimated values of the ratio m/m_{ii} in the directions of drag and lift are shown in figure 12(*b*). These values have been computed numerically from the measured time-dependent data of drag and lift and the corresponding longitudinal and normal accelerations during the deployment of the flap by using (9.4). First, the results clearly show that the added masses associated with the longitudinal and normal forces and accelerations are reduced with increasing *Str*. Second, it appears that m_{11} and m_{22} are quantitatively different from each other. In the case of the drag force, the impulse of the inertia force $m\,\mathrm{d}^2x_1/\mathrm{d}t^2$ is always less than I and at most it can be $0.6I$ at $Str = 0.23$, while in the case of lift it is about $1I$ at small *Str* or exceeds this value substantially at high *Str*. The impulse of the driving force is estimated to be proportional to T_s/ω where T_s is the maximum torque (stall torque) of the motor at no rotation while I is at most proportional to $1/\omega$. Thus, it can be argued that the ratio I_{drive}/I varies as T_s which is proportional to the control voltage V provided to operate the servomotor at a given load. This voltage increases with the increasing aerodynamic loads and therefore the right-hand side of (9.13) increases with *Str* in the same way that the ratio m/m_{ii} increases in the left-hand side of (9.13). Since the voltage V required to drive the actuator in each case was not recorded and the terms I_c/I and I_k/I of the mechanical system were not considered in the present analysis, it is not possible to quantitatively verify (9.13).

Another characteristic of the impulse data in figure 12(*a*) is that the actual momentum input in the flow is greatly influenced by the shape of the actuator. This is actually a byproduct of the area ratio since the area of the triangular panel is half that of the square one, the momentum input to the flow is also approximately half.

Figure 12(*a*) also shows that the actual momentum input to the flow is affected very marginally by the height of the boundary layer. The relatively small differences that can be observed in the results occur only at high *Str*.

10. Interaction between the actuator and boundary layer structures

The present flow can be considered as the result of a continuous transient interaction between a deploying actuator with a well-described and controlled motion and the incoming boundary layer and irrotational free stream flow. The boundary layer contains turbulent structures with considerable degree of spatial and temporal randomness and 'entrained free stream' fluid which undergoes transition from irrotational to rotational state. As a consequence of the randomness present in the input flow of this interaction, its output is dynamic and the instantaneous structure of the flow is very different even from the 'phase-locked' averaged structure let alone the long time-averaged flow.

During the deployment of the actuator the upstream turbulent boundary layer structures (BLSs) and the free-stream fluid are decelerated and squeezed in the longitudinal direction and stretched in the lateral direction as they approach the moving plate. At the same time a horseshoe vortex (HV) starts to form over the moving plate and move upstream during the final stages of deployment while the incoming boundary layer turbulent structures are pushed and diverted upwards. These structures flow over the upper part of the plate as they form a very thin and highly sheared wall layer developing over the moving upstream surface of the plate. This generates a substantial amount of vorticity by the action of pressure gradients at the wall and its own motion as described by (1.2*a*) and (1.2*b*). This highly sheared wall layer is not a conventional boundary layer since it is immensely disrupted by large external disturbances with scales much larger than its thickness. Its structure is very intermittent because it is part-time turbulent and part-time laminar depending on whether a turbulent eddy from the incoming large-scale boundary layer or laminar 'entrained free stream' fluid is touching the moving plate and interacts with it. These pockets of turbulent eddies and free stream fluid are highly compressed and leave the moving surface in the form of a separated shear layer which rolls up to form large-scale vortical structures in the area between the wake and the free stream named hereafter a tip vortical structure (TVS). A TVS consists of many layers of piled up compressed and sandwiched incoming boundary layer eddies and free stream pockets. It is these structures which are responsible for the generation of the additional dynamic lift.

In the following, the results of our flow visualization studies will be presented and discussed. The CW laser sheet was first aligned normal to the spanwise direction at two different locations at $x_3 = 0$ and $x_3 = -3$ cm from the origin while the camera was positioned outside the wind tunnel as shown in figure 13(*a*). Subsequently the laser sheet was aligned parallel to the wall at heights $x_2 = 9$ and $x_2 = 2$ cm from the wall and the camera was mounted on the top of the wind tunnel viewing the flow through a window as shown in figure 13(*b*).

The most significant feature of the interaction of the moving panel with the incoming flow developing over the upstream wall is the generation of vortical
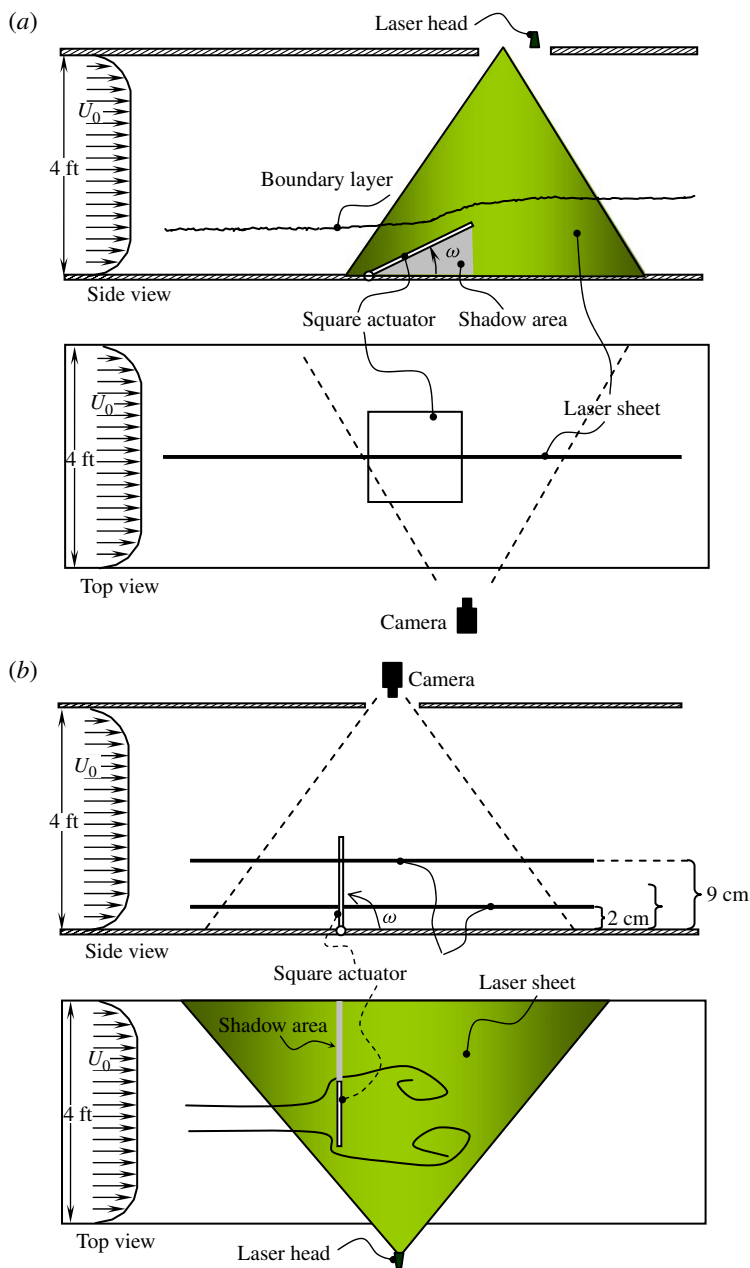
FIGURE 13. (Colour online) (*a*) Flow visualization set-up with illumination by a vertical laser sheet. Boundary layer thickness $\delta = 5$ cm, $U_0 = 10.69$ m s^{-1}, 10 cm $\times$ 10 cm square panel. Schematic not to scale. (*b*) Flow visualization setup with illumination by a horizontal laser sheet. Boundary layer thickness $\delta = 5$ cm, $U_0 = 10.69$ m s^{-1}, 10 cm $\times$ 10 cm square panel. Schematic not to scale.
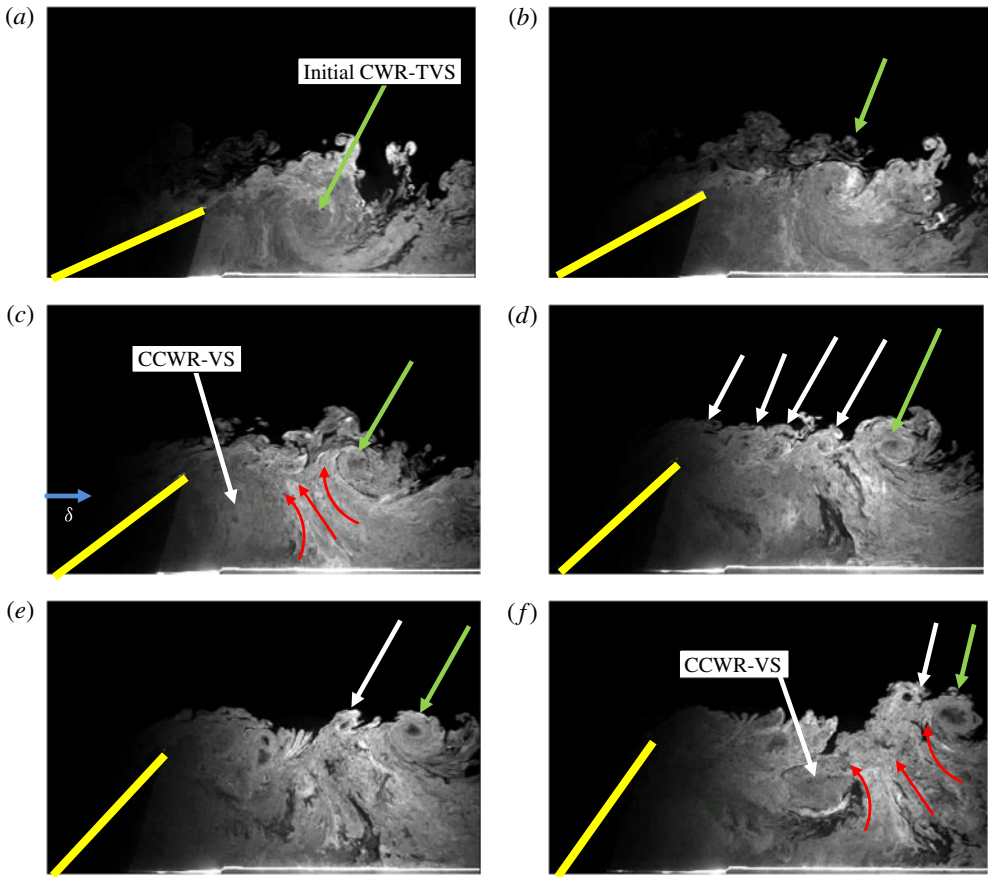
FIGURE 14. (Colour online) Vortical structures shed off the tip of the actuator, during deployment angles 22 to 55°. Grey arrows (shown in green online) refer to initial CWR-TVS, images taken at $x_3 = 0$ plane ($Re_\theta = 3400$; $Re_h = 68\,200$; $Str = 0.24$). Horizontal arrow indicates boundary layer thickness δ.

structures shed off the tip of the rotating panel. The evolution of the flow structures is shown in the attached video which has been obtained with a rate of 3000 frames s^{-1} (see movie 1 available at http://dx.doi.org/10.1017/jfm.2013.52.). This frame rate allowed tracking of individual vortical structures and monitoring their interaction with the flow.

A sequence of six flow visualization images obtained at specific phases of the rotation is shown in figure 14. The moment the panel starts its motion relatively to the flow, it generates additional vorticity at each of its two faces beyond the preexisting one of the incoming boundary layer.

As the boundary layer separates the panel at its tip, an undulated shear layer is formed that tends to roll and wrap around itself by the motion induced by the inrushing reverse flow in the wake. This clockwise rotating tip vortical structure (CWR-TVS) consists of several bands of the separated thin shear layer and it carries strong clockwise rotating circulation. It grows substantially with time and at deployment angle of 22° has a size of the order of the panel height as shown in figure 14(*a*). One additional characteristic of this structure is that it moves downstream
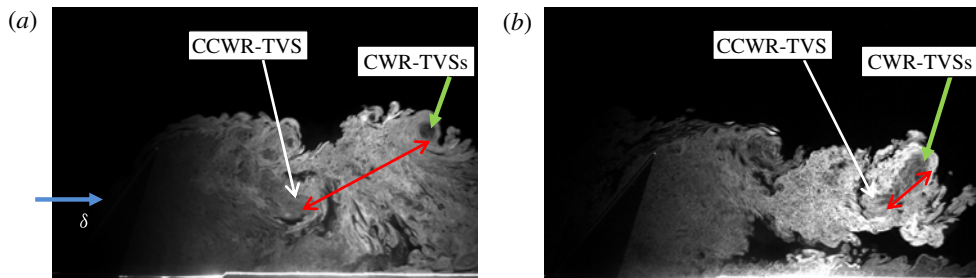
FIGURE 15. (Colour online) Comparison of flow structures between images: (*a*) flow visualization with a laser sheet at $x_3 = 0$ cm with the flap at 55° deployment; (*b*) flow visualization with a laser sheet at $x_3 = -3$ cm with the flap at 48° deployment. Flow with $Re_\theta = 3400$; $Re_h = 68\,200$ and $Str = 0.24$. Double-headed arrows (shown in red online) show the distance between the centres of vortical structures.

very slowly. At later times a vortical structure with counterclockwise rotation appears (CCWR-TVS) in the flow close to the moving panel. In between the two counter-rotating structures fluid is erupted upwards suggesting the existence of a larger-scale mushroom-type vortical structure. This upward moving fluid is fed by the intense flow inrush over the stationary wall, which is directed towards the low-pressure region developing in the wake of the moving panel. As is shown in figure 14(*f*), the distance between the CWR-TVS and CCWR-TVS is close to the panel height, *h*.

As the panel is further deployed, additional TVSs are evident in the flow which move upwards and in the downstream direction. Four large-scale CWR-TVSs are shown in figure 14(*d*) interconnected in a street-like arrangement along the separated shear layer. It is the formation of the TVSs and the vorticity shed off the front face of the rotating panel which are responsible for the generation of the dynamic lift and drag forces. After the end of the deployment, the shear layer is not wrapped around itself anymore and it appears as an non-undulated shearing region between the faster moving free stream flow above and the wake of the panel below.

Of great interest are the questions whether these TVSs, which are responsible for the augmented force generation, are present at locations off the plane of symmetry $x_3 = 0$ and what is their lateral extent? In order to answer these questions the laser sheet was moved to the position $x_3 = -3$ cm off the centre plane. Figure 15 shows a comparison of the image: (*a*) obtained at $x_3 = 0$ cm with the image; (*b*) obtained at the $x_3 = -3$ cm plane. In both images, a CWR-TVS bundled with a CCWR-TVS can be identified with the distance between them being much smaller at $x_3 = -3$ cm.

Most probably, both the CWR and the CCWR parts belong to the same leg of a vortical structure which has a circular shape and the CCWR part is the result of a cross section of the same vortical structure. Such a three-dimensional vortical structure may have been formed by the concurrent shedding of shear layer vorticity around the whole perimeter of the panel that includes not only the top edge but also its two lateral edges with each of them shedding vorticity oriented on a vertical plane. This structure as it moves downstream becomes more circular and because of the inrush of lateral fluid towards the low-pressure wake of the panel, the lower tips of its two legs are re-orientated towards the middle plane giving the shape of an open ring. This shape can definitely explain the appearance of the two opposite rotating vortical structures visualized by the planar laser sheet at $x_3 = -3$ cm and $x_3 = 0$.
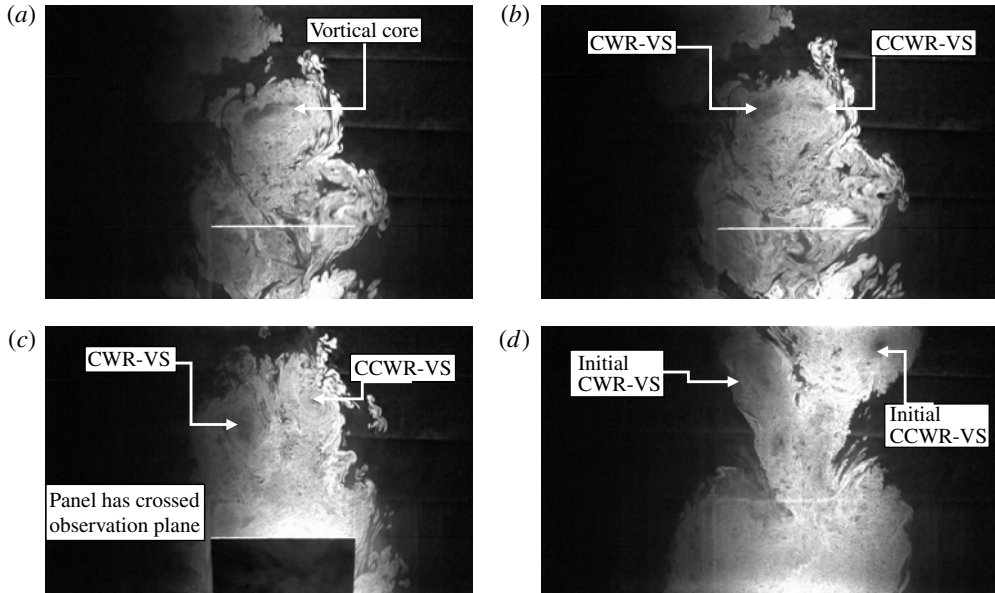
FIGURE 16. Flow visualization with laser sheet at $x_2 = 9$ cm and flow with $Re_\theta = 3400$, $Re_h = 68\,200$ and $Str = 0.24$: (*a*) panel at 63° deployment; (*b*) panel at 63.2° deployment; (*c*) panel at 65° deployment; (*d*) panel at 73° deployment.

One additional characteristic is that their distance decreases away from the plane of symmetry as indicated in figure 15 which is consistent with the ring structure.

In order to test this hypothesis the laser sheet was turned to become parallel to the tunnel wall and two additional flow visualization experiments were carried out. The evolution of the flow structure as a function of deployment/time can be observed in the video stored (see movie 2). Figure 16 show some representative images at specific deployment angles. When the panel is at 63° (image figure 16*a*) the appearance of a low-concentration tube is observed which, most probably, is associated with the core of the vortical structure shed off the horizontal edge of the panel. This vortex core is connected to the two counter-rotating structures visualized in the next image figure 16(*b*) with the panel at 63.2° deployment angle. The two structures move apart away from each other in the frame shown in image figure 16(*c*) when the panel is at 65°. At this time the panel had crossed the laser sheet. Movie 2 shows clearly a strong induced reversed flow between the two counter-rotating structures at the plane of symmetry. The distance between the two structures seems to increase with time, a feature consistent with a vortex ring moving upwards. The two structures are been transported slowly by the flow in the downstream direction while there is a stenosis of the visualized wake behind them, as shown in figure 16(*d*), which is associated with the inrushing fluid form the two lateral directions towards the plane of symmetry where the pressure is very low. Finally this stenosis is further stretched by the reverse flow as is shown in movie 2 and becomes quite narrow at 83° deployment while large vortical structures are formed through wrapping around of the shear layers shed off by the two lateral edges of the panel. While this open ring-like structure has been observed at the $x_2 = 9$ cm plane of visualization, it was not possible to identify any coherent pattern of rotating structures at the $x_2 = 2$ cm plane when the laser sheet was
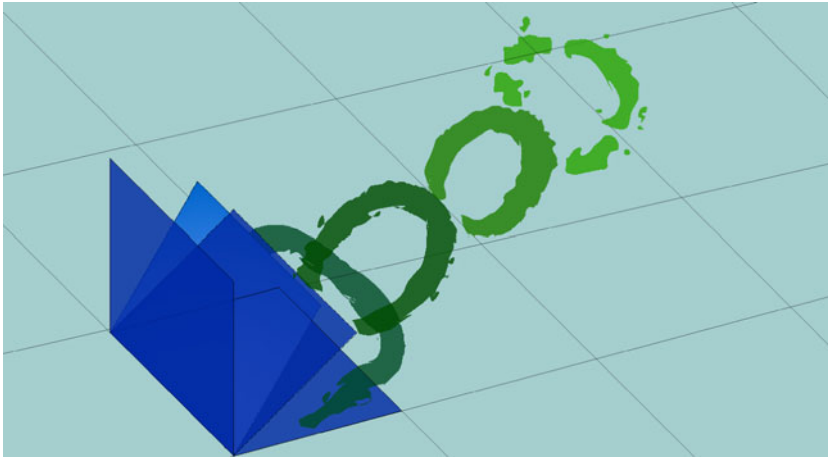
FIGURE 17. (Colour online) Evolution of the conceptual TVS.

moved closer to the wall. This may be due either to the strong interaction of these structures with the near-wall turbulence which may have completely distorted their rotational characteristics or the vorticity carried by these structures may be rather weak at the close to the wall parts of the two lateral edges of the panel.

Figure 17 shows a highly simplified concept of the TVS as it is evolving with time that is consistent with the visual evidence observed in the visualization studies. It contains the major features only with many details left out. The three-dimensional highly shear wall layer developing over the front face of the moving panel separates from the top and side edges of the panel to form a shear layer which wraps around itself to form an open ring-like vortical structure. This structure consists of many layers of piled up incoming boundary layer eddies which are compressed and sandwiched to form several bands around it. It is this structure in its totality which is mostly responsible for the augmented force generation, not the individual sandwiched eddies of the upstream boundary layers, which are its building blocks. It is also worth mentioning that this structure is not a laminar vortex in its classical definition. It is a wrapped around shear layer which possesses strong rotation and consists of turbulent eddies as well as of pockets of entrained free stream fluid contained in bands around it. There is some strong interaction of the TVS with turbulence in the near-wall region and in the wake of the moving panel as it slowly moves downstream. While these vortical structures were always detectable in the near wake of the moving panel in all Re cases, it was not possible to identify them in distances far downstream. In the highest Re case investigated, for instance, some individual CWR-TVS structures were observed in distances greater than 6 h travelling downstream with the free stream velocity but never in pair with a CCWR. This clearly suggests that some significant distortion or a breakup of the structure associated with some loss of coherence occurs which makes the structures discontinuous.

One obvious question is how this single structure, initially identified as an open ring, relates to structures observed in other impulsively accelerating flows or flapping motions of panels in non-wall-bounded flows or in the propulsive wakes of fish and other marine mammals. In all of these cases as well as in the present flow vorticity is shed in the wake from three edges of the flapping panels. As a result of the relative length of the edges, i.e. their aspect ratio, the vortex structure can be dominated by

two tip vortices if the side edges are longer or the top vortex if the top edge is wider in the spanwise direction. Thus, the flapping panel geometry plays a significant role in the formation of the initial structure together with the dynamic boundary conditions which are mainly characterized by the *Str*.

We have recently completed some quantitative measurements by using our time-resolved PIV techniques with a CW laser and a fast frame rate camera which agree with our qualitative observations. The measured time-resolved vorticity identified all of the vortical structures described above. This work which is the second author's PhD Thesis (Elzawawy 2012) will be part of another manuscript under preparation together with the some theoretical work.

The present qualitative and quantitative results appear to have some similarities to the conclusions and observations of Ringuette *et al.* (2007) despite the difference in Reynolds numbers between them. The LEV formed during the impulsive translation of normal to the flow panels resembles the present CWR-TVS while the tip vortices found in the study of Ringuette *et al.* (2007) are longer and play a more important role in the dynamics of drag generation. In the present case with an impulsively rotating panel, most of the contribution to the transient lift generation comes from the top spanwise part of the CWR-TVS than from the tip vortices.

Additional common features regarding the dynamics of these tip vortices can be found in the way they move in the wake of the panel. It has been observed in both flows that the inrushing fluid from the sides towards the low-pressure region in the near wake causes them to approach each other very close in the spanwise direction. As they move further downstream their distance starts to increase.

Another remarkable similarity between the present flow and that of Ringuette *et al.* is the dynamic development of the drag force. The *Cd* data shown in figure 8(*a*) are qualitatively similar to the *Cd* data of Ringuette *et al.* presented in figure 2 of their paper although the initial increase close to the beginning of the dynamic effects is not well resolved.

Similarities of the present flow structure are not limited to accelerating panels only. A comparison with the wake structure model of flapping panels observed by Buckholtz & Smits (2006, 2008) indicates strong similarities of the present rendering with the structure shed off during the first quarter of the flapping cycle at about the same *Str* number. Owing to the low aspect ratio of panels used in these experiments their HV model has longer streamwise vortices than those observed in the present study. However, most of the dynamics of the motion and the associated interactions are dominated by the vorticity in the vortex sheet connecting the two streamwise vortices. Similar behaviour has been observed in the present CWR-TVS which is mostly associated with the dynamic drag and lift generation.

Ring type of structures have been also observed in the near wake of fish tail flapping motions as shown in the high-*Re* cases computations of virtual swimmers by Borazjani & Sotiropoulos (2010). At *Str* = 0.3 all swimmers shed a single row structure and the case of lamprey shows an initial structure similar to the present ring structure. However, fish tails have more than three edges shedding vorticity, a feature which inhibits further comparison of the structures.

The presence of the wall upstream and downstream of the panel is the main attribute which distinguishes the present flow from all of these studies mentioned above. The upstream wall generates the incoming boundary layer turbulence which alters the detailed structure of the vortical systems particularly during the initial stages of the deployment and the downstream wall affects the wake development. As a result, the separated shear layers in the present case consist of pockets of compressed turbulent

eddies originated in the boundary layer upstream and free stream fluid which are wrapped around to form the vortical structures. The shear layers of Ringuette *et al.* (2007) undergo a Kelvin–Helmholtz (KH) instability first before they form the tip vortex and LEV. This is also the difference between the present CWR-TVS and the vortices in the high-Reynolds-number wake of a cylinder shown in the recent works of Dong *et al.* (2006) and Akaydin, Elvin & Andreopoulos (2010). Shear layer vortices are formed in the wake of the cylinder as a result of KH instability which grow in size and eventually are wrapped around the main large-scale Kármán vortices.

11. Upstream effects during deployment

A series of flow visualization experiments were conducted focusing on the incoming boundary layer flow upstream of the panel. A video can be seen in movie 3. Figure 18 shows a sequence of 11 images extracted out of this video during the panel deployment. The evolution of a typical large-scale BLS at $Re_\theta = 3400$ is depicted in the first image as it approaches the deploying actuator. A compressive straining of the BLS can be observed in the longitudinal direction while an expansive straining in the lateral direction is present as the fluid is decelerated in the longitudinal direction and then it is diverted over the panel or in the lateral directions. It is also evident that a stagnation point occurs when the panel is at $57.5°$ (figure 18(1)) at a distance of about $x_2 \approx 1/5h$ from the wall. The flow below that point starts to separate and a recirculatory motion is observed at the root of the panel which eventually leads to the appearance of a HV upstream of the panel with flow separation above the stationary wall of the wind tunnel. This stagnation point moves upwards to about $0.3h$ as the deployment progresses and the HV is more visible.

As this particular BLS is decelerated and compressed to a much thinner structure as it goes over the rotating panel, it wraps around the CWR-TSV generated at its tip as a very thin layer while there is a dark unseeded layer of free steam fluid between this and the proceeding structure. Thus, the CWR-TSV is a rotating multi-layer structure formed by sandwiching piled up upstream BLSs.

The HV is clearly evident in several of the images of figure 18. As the typical BLS approaches the moving panel first interacts with the HV at about a distance of $x_1/h = -0.4$ and then it starts to be compressed in the streamwise direction. Eventually it reaches the moving plate and it is swept away in the shear wall layer upwards towards the tip where it separates. This HV during the final stages of the panel deployment and immediately after when the flow adjusts to a steady-state development has the characteristics of the turbulent HV described by Agui & Andreopoulos (1992) for the case of a high-Reynolds-number three-dimensional turbulent boundary layer flow formed in front of a wall-mounted cylinder. The HV in the present flow wonders considerably in both longitudinal and normal directions while exhibiting an intermittent strength which induces the generation of opposite rotating vortices at the wall that are part of similarly occurring eruptive phenomena observed in several flows where a vortex interacts with a stationary boundary. Paik, Escauriaza & Sotiropoulos (2007) argue that these phenomena could be the result of centrifugal instability due to the combination of the local streamline curvature imposed by the vortex and the inflection point in the velocity profile caused by the proximity of the vortex to the wall. The major difference between the present boundary layer dynamics upstream of the rotating panel and those upstream dynamics reported in the literature of stationary wall-mounted obstacle is that the extent of the upstream influence region has been observed to grow continuously with the deployment time
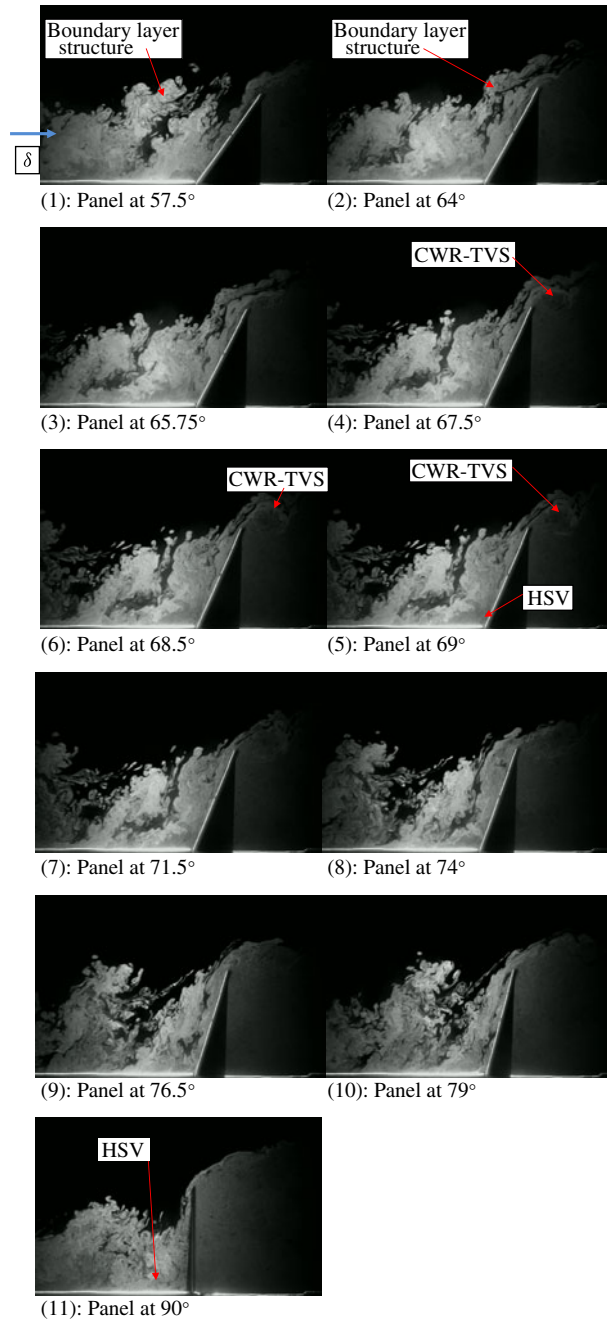
FIGURE 18. (Colour online) Images (1)–(11) show a sequence of flow visualization during the interaction of the deploying actuator with the incoming boundary layer flow obtained in flow with $Re_\theta = 3400$, $Re_h = 68\,200$ and $Str = 0.24$. The arrow δ (shown in blue online) shows the boundary layer thickness.

and it appears to grow even after the end of the deployment for a short time. In particular, the HV travels upstream as the panel rotates and reaches a location of maximum upstream distance much after the deployment has stopped which is about twice the average steady-state location. The onset of new flow conditions imposed by the stationary now panel brings the HV back towards the panel to its final location where it starts to wander around as it interacts with the local turbulent structures. This monotonic upstream movement of the HV while the actuator is in motion and its time delay in adjusting its location to the new steady-state boundary conditions have been observed consistently and they constitute the main difference between the present transient upstream dynamics and the dynamics of the steady state. The eruptive phenomena including the generation of opposite rotating vortices at the wall observed in the steady-state dynamics are also visible during the later phases of the unsteady motion when the length and time scales of the flow grow substantially as the flow is being transformed from a two-dimensional boundary layer to a three-dimensional stagnating flow.

Of interest is the question of what is the role, if there is any, of the HV in the transient generation of the aerodynamic forces? The $Str = 0.03$ case has shown the development of a HV during the last stages of the actuator deployment with very minimal dynamic drag above its static one. In that respect, there is no evidence that the HV contribute to the generation of excess dynamic forces on the panel. In general, the HV affects the late stages of the flow dynamics during the panel deployment and the steady-state flow structure after the end of the deployment. It appears that it reduces the steady-state drag by diverting upwards the incoming boundary layer fluid, part of which does not decelerate to stagnation on the front face of the plate itself. In fact in our wall-proximity studies, it has been found that the Cd is considerable less when the plate touches the wall than its corresponding value when the plate is far away from the wall. Part of this reduction in Cd is due to momentum losses associated with the incoming upstream boundary layer and part is due to the HV formation upstream of the normal to the wall plate.

12. Conclusions

An experimental investigation has been carried out to demonstrate the characteristics of wall-mounted rotating actuators/panels during their transient deployment. Triangular and square planform actuators were used in the present experimental investigation. Each planform was tested in five different rotational speeds/velocity ratios and two different boundary layers. The deployment angular velocity was kept constant during the cycle except in the beginning and the end of it where substantial accelerations were observed. Our experimental results indicated an increase in the magnitude of the aerodynamic forces that are generated during the transient deployment of the panels beyond the corresponding steady-state values. It appears that these dynamic effects increase with increasing the velocity ratio Str. The square actuator was found to have better aerodynamic performance than the delta or triangular actuators in terms of actual force values and the corresponding force coefficients. Integration of the measured forces over time indicated that their impulse is reduced with increased velocity ratio with square panels having always larger impulses than the corresponding triangular shape ones at the same Str.

Experiments at two different locations in the same boundary layer flow established the effect of the boundary layer thickness on the generated forces. It was found that for the same nominal velocity ratio the thinner the boundary layer is the higher the

dynamical effects and therefore the higher the forces are. The present results also showed that the impulse of the aerodynamic forces is not considerably affected by the thickness of the incoming boundary layer.

Extensive time-resolved visualization studies of the flow around the actuators during their deployment revealed details of their interaction with the incoming turbulent boundary layer and the free stream flow. A shear layer emanating from the tip of the panel was observed during the early stages of deployment to wrap around itself to form a large-scale ring-like turbulent vortical structure which consists of layers of highly compressed turbulent eddies originated in the upstream incoming wall boundary layer flow. This layered structure which is associated with the unsteady generation of aerodynamic forces interacts with the turbulence in the wake of the moving panel while it is growing in size and moving very slowly upwards and in the downstream direction before it is swept downstream very fast. Vorticity is continuously generated and shed off the front surface of the panel in the form of large-scale vortical structures until about a few degrees of deployment angle before the panel arrests its motion.

A HV is always observed in front of the panel starting to form at very small deployment angles. This vortex does not contribute to the generation of unsteady forces. However, it reduces the value of the steady-state drag force.

Acknowledgement

Supplementary movies

Supplementary movies are available at http://dx.doi.org/10.1017/jfm.2013.52.

REFERENCES

AGUI, J. H. & ANDREOPOULOS, J. 1992 Experimental investigation of a three-dimensional boundary layer flow in the vicinity of an upright wall mounted cylinder. *Trans. ASME J. Fluids Engng* **114** (4), 566–576.

AKAYDIN, D. H., ELVIN, N. & ANDREOPOULOS, Y. 2010 Wake of a cylinder: a paradigm for energy harvesting with piezoelectric materials. *Exp. Fluids* **49** (1), 291–304.

ANDERSON, J. M., STREITLIEN, K., BARRETT, D. S. & TRIANTAFYLLOU, M. S. 1998 Oscillating foils of high propulsive efficiency. *J. Fluid Mech.* **360**, 41–72.

ANDREOPOULOS, J. & AGUI, J. 1996 Wall vorticity flux dynamics in a two-dimensional turbulent boundary layer. *J. Fluid Mech.* **309**, 45–84.

BIRCH, J. M. & DICKINSON, M. H. 2001 Spanwise flow and the attachment of the leading-edge vortex on insect wings. *Nature* **412** (6848), 729–733.

BORAZJANI, I. & SOTIROPOULOS, F. 2010 On the role of form and kinematics on the hydrodynamics of body/caudal fin swimming. *J. Expl Biol.* **213**, 89–107.

BUCKHOLTZ, J. H. J. & SMITS, A. J. 2006 On the evolution of the wake structure produced by a low-aspect-ratio pitching panel. *J. Fluid Mech.* **546**, 433–443.

BUCKHOLTZ, J. H. J. & SMITS, A. J. 2008 The wake structure and thrust performance of a rigid low-aspect-ratio pitching panel. *J. Fluid Mech.* **603**, 331–365.

DICKINSON, M. H., LEHMANN, F. O. & SANE, S. P. 1999 Wing rotation and the aerodynamic basics of insect flight. *Science* **284**, 1954–1960.

DONG, S., KARNIADAKIS, G. E., EKMEKCI, A. & ROCKWELL, D. 2006 A combined DNS-PIV study of the turbulent near wake. *J. Fluid Mech.* **569**, 185–207.

VON ELLENRIEDER, K. D., PARKER, K. & SORIA, J. 2003 Flow structures behind a heaving and pitching finite-span wing. *J. Fluid Mech.* **490**, 129–138.

ELLINGTON, C. P. 1984 The aerodynamics of hovering insect flight. II. Morphological parameters. *Phil. Trans. R. Soc. Lond.* **305**, 17–40.

ELLINGTON, C. P., VAN DEN BERG, C., WILLMOTT, A. P. & THOMAS, A. L. R. 1996 Leading-edge vortices in insect flight. *Nature* **384** (6610), 626–630.

ELZAWAWY, A. 2012 Time resolved particle image velocimetry techniques with continuous wave laser and their application to transient flows. PhD thesis, The City University of New York.

FREYMUTH, P. 1988 Propulsive vortical signature of plunging and pitching aerofoils. *AIAA J.* **23**, 881–883.

GREEN, M. A. & SMITS, A. J. 2008 Effects of three-dimensionality on thrust production by a pitching panel. *J. Fluid Mech.* **615**, 211–220.

HO, C. H. & TAI, Y.-C. 1998 Micro-electro-mechanical systems (MEMS) and fluid flows. *Annu. Rev. Fluid. Mech.* **30**, 579–612.

HO, S., NASSEFA, H., PORNSIN-SIRIRAK, N., TAI, Y.-C. & HO, C.-M. 2003 Unsteady aerodynamics and flow control for flapping wing flyers. *Prog. Aeronaut. Sci.* **39**, 635–681.

KIM, D. & GHARIB, M. 2010 Experimental study of three-dimensional vortex structures in translating and rotating plates. *Exp. Fluids* **49** (1), 329–339.

KOUMOUTSAKOS, P. & SHIELS, D. 1996 Simulations of the viscous flow normal to an impulsively started and uniformly accelerated flat plate. *J. Fluid Mech.* **328**, 177–227.

MAXWORTHY, T. 1981 The fluid-dynamics of insect flight. *Annu. Rev. Fluid Mech.* (13), 329–350.

PAIK, J., ESCAURIAZA, C. & SOTIROPOULOS, F. 2007 On the bimodal dynamics of the turbulent horseshoe vortex system in a wing-body junction. *Phys. Fluids* **19**, 045107.

PIERIDES, A. 2011 An experimental study on the characteristics of transient deployment of hinged wing actuators within a boundary layer. PhD thesis, The City University of New York.

RINGUETTE, M. J., MILANO, M. & GHARIB, M. 2007 Role of tip vortex in the force generation of low-aspect-ratio normal flat plates. *J. Fluid Mech.* **581**, 453–468.

SARPKAYA, T & KLINE, H. K. 1982 Impulsively-started flow about four types of bluff body. *Trans. ASME I: J. Fluids Engng* **104**, 207–213.

SURYADI, A., ISHIL, T. & OBL, S. 2010 Stereo PIV measurement of infinite, flapping rigid plate in hovering condition. *Exp. Fluids* **49** (2), 447–460.

TAIRA, K., DICKSON, W. B, COLONIOUS, T., DICKINSON, M. H. & ROWLEY, C. W. 2007 Unsteadiness in a flow over a flat plate at angle-of-attack at low Reynolds numbers, AIAA-65342 conference paper.

TRIANTAFYLLOU, M. S., TECHET, A. H., ZHU, Q., BEAL, D. N., HOVER, F. S. & YUE, D. K. P. 2003 Vorticity control in fish-like propulsion and control. *J. Integ. Comp. Biol* **42**, 1026–1031.

TRIANTAFYLLOU, M. S., TRIANTAFYLLOU, G. S. & GOPALKRISHNAN, R. 1991 Wake mechanics for thrust generation in oscillating foils. *Phys. Fluids* A **3** (12), 2835–2837.

VIKESTAD, K., VANDIVER, J. K. & LARSEN, C. M. 2000 Added mass and oscillation frequency for a circular cylinder subjected to vortex-induced vibrations and external disturbance. *J. Fluids Struct.* **14**, 1071–1088.

WANG, Z. J. 2005 Dissecting insect flight. *Annu. Rev. Fluid Mech.* **37**, 183–198.